

INVESTIGATION ON THE MACHINABILITY IN THE  
MICRO-MILLING OF AMORPHOUS MATERIALS

By

BOYUAN XIE

Bachelor of Science in Mechanical Engineering

Dalian Jiaotong University

Dalian, Liaoning, China.

2010

Submitted to the Faculty of the  
Graduate College of the  
Oklahoma State University  
in partial fulfillment of  
the requirements for  
the Degree of  
MASTER OF SCIENCE  
July, 2016

## ACKNOWLEDGEMENTS

First, I would like to express my sincere gratitude to my advisor Dr. Xiaoliang Jin for the guidance, encouragement, and continuous support through the whole process of my M.S. study and related research. His guidance helped me in right directions of my research and writing this thesis.

I would also like to thank the rest of my thesis committee: Dr. Don A Lucca and Dr. Sandip P. Harimkar, not only for their support for my research, but also for their encouragement, which inspired me to widen my research from various perspectives. Without their precious support it would not be possible to conduct this research.

In addition, I would like to thank S. Habib Alavi for his help on using the profilometer, Dr. Lu for his help on using the SEM and XRD, and the customer services from PI, Accel instruments, Fischer Precise for their help in building new machining system for my research.

My sincere thanks also go to my colleagues Anju, Arjun, Gopal, Naresh, Keeley, Vinay and Lingwei in our lab. No matter when I needed help, they were always there.

Finally, I would like to especially thank my parents for their support as I love them always; Also my aunt Holly, who made my life in the United States much easier.

Name: BOYUAN XIE

Date of Degree: JULY, 2016

Title of Study: INVESTIGATION ON THE MACHINABILITY IN MICRO-MILLING OF AMORPHOUS MATERIALS

Major Field: MECHANICAL AND AEROSPACE ENGINEERING

Abstract:

Amorphous materials have been widely used in various industrial areas such as optics, aerospace, sports, and biomedical applications. The fundamental mechanism in machining amorphous materials is different from that in machining metallic materials due to their unique microstructure and mechanical properties. This thesis presents experimental investigations on the machinability in the micro-milling of two typical amorphous materials: Zirconium based bulk metallic glass (Zr-BMG) and BK-7 glass.

A three-axis micro-milling machine is developed to perform the machining experiments on Zr-BMG with a spindle speed of up to 105,000 rpm. The effect of cutting conditions on light emission and surface melting in the micro-milling of Zr-BMG is investigated. The microstructure and crystallization of machined surface are characterized using scanning electron microscopy, metalloscope, X-ray diffraction and Energy Dispersive Spectroscopy. The critical cutting conditions that correspond to the onset of surface crystallization are determined. Progressive tool flank wear with respect to the cutting distance with and without coolant is also analyzed.

A resonance based two dimensional vibration stage with thin-wall design is developed to perform the vibration assisted micro-milling of brittle BK-7 glass. The dynamic property of the vibration stage is analyzed using the finite element method and experimental identification. The effects of vibration direction, vibration amplitude and frequency on the surface roughness and surface damage are investigated. It is concluded that the vibration applied in the normal direction has a major effect on the improvement of surface quality by enhancing the brittle-ductile transition of the material in the micro-milling process.

**Keywords:** Micro-milling, amorphous material, bulk metallic glass, BK-7 glass, machinability

## TABLE OF CONTENTS

Chapter	Page
I. INTRODUCTION .....	1
1.1. Background.....	1
1.2. Objective and Approach .....	3
II. LITERATURE REVIEW .....	5
2.1. Machining of Bulk Metallic Glass.....	5
2.2. Machining of Optical Glass .....	8
2.3. Vibration Assisted Machining for Brittle Materials .....	9
2.3.1. Vibration Assisted Machining System .....	9
2.3.2. Benefits of VAM for brittle materials .....	11
2.4. Summary.....	13
III. MACHINABILITY IN MICRO-MILLING OF ZIRCONIUM BASED BULK METALLIC GLASS.....	15
3.1. Overview.....	15
3.2. Experimental Setup.....	15
3.2.1. Description of the experimental setup.....	15
3.2.2. Development of high spindle speed micro-milling machine.....	17
3.3. Experimental Process of Micro-milling of Zr-BMG .....	22
3.3.1. Light emission in the micro-milling process .....	22
3.3.2. Characterization of machined surface by SEM and metalloscope .....	25
3.3.3. Crystallization of workpiece material .....	27
3.3.4. Tool wear in micro-milling of Zr-based BMG.....	33
3.3.4.1. Tool wear in dry machining condition.....	33
3.3.4.2. Tool wear in machining with mist coolant .....	36

3.4. Summary.....	37
<b>IV. VIBRATION ASSISTED MILLING OF BK-7 GLASS .....</b>	<b>39</b>
4.1. Overview.....	39
4.2. Design of the 2-D Vibration Stage .....	40
4.2.1. Vibration source .....	41
4.2.2. Type of vibration system.....	41
4.2.3. Design of vibration stage.....	43
4.2.4. Vibration stage vibration analysis .....	45
4.2.5. Identification of the dynamic property .....	49
4.3. Experimental setup .....	51
4.4. Machining Mechanism of Vibration Assisted Milling Process .....	52
4.5. Experimental Process.....	54
4.6. Experiment Result .....	55
4.6.1. Measurement of surface quality .....	55
4.6.2. Result and analysis .....	56
4.7. Summary.....	59
<b>V. CONCLUSIONS AND RECOMMENDATIONS .....</b>	<b>61</b>
5.1. Conclusion .....	61
5.2. Recommendations for Future Work .....	62

## LIST OF TABLES

Table	Page
3.1 Composition of LM105 Bulk Metallic Glass .....	16
3.2 Mechanical Properties of LM105 Bulk Metallic Glass.....	16
3.3 Specification of Linear Stage .....	17
3.4 Specification of Spindle .....	18
3.5 Light Emission Level in Different Experiments .....	23
3.6 Critical Cutting Conditions for Crystallization Transition.....	32
4.1 (a) Specification for P844.10 Piezo Actuator (b) Required Vibration Parameters .....	42
4.2 Vibration Stage Material Properties.....	45
4.3 Vibration Stage Mode Shapes under 20 kHz .....	48
4.4 CPL-290 Specification.....	49
4.5 BK7 Specification.....	52
4.6 Cutting Conditions .....	55
4.7 Surface Profile Measured by Optical Profilometer .....	59

## LIST OF FIGURES

Figure	Page
1.1 Application of Micro-optics (a) Telescope (3.6 mm diameter and 4.4 mm length) (b) Camera (5.9 mm by 5.8 mm by 2.25 mm) (c) Micro-lens (70 $\mu\text{m}$ diameter) (d) Hemi-elliptical Micro-lenses (284 $\mu\text{m}$ length) .....	1
1.2 BMG Product (a) Golf Clubs (b) Cellphone Case .....	2
1.3 Comparison of 1-D and 2-D Vibration (a) 1-D (b) 2-D .....	3
2.1 X-ray Diffraction Result for As-received, Machined Surface and Chips .....	7
2.2 Optical Micrographs of Cross-Section of Chip (a) Crystallization Incipient near the Oxide Layer, (b) Transition from Crystalline (Left) to Amorphous (Right) Regions, (c) Dendritic Crystalline Branch and the Maximum Cooling Rate Directions Indicated by Arrows, and (d) Fully Crystalline Region .....	7
2.3 Machining Geometry Used to Derive the Cutting Model .....	8
2.4 Vibration Motion of (a) 1-D VAM (b) 2-D VAM .....	10
2.5 VAM System (a) 1-D (b) 2-D .....	11
2.6 SEM Photographs of Nano-ZrO <sub>2</sub> after (a) Conventional Diamond Grinding (b) 2-D Ultrasonic Assisted Grinding .....	13
3.1 (a) MDA Precision Micro-Machining Center (b) High Speed Machining system .....	16
3.2 Coolant System (a) Dispenser (b) Sink .....	17
3.3 Schematic of High Speed Machining System .....	19
3.4 Alignment of Z-axis .....	20
3.5 Alignment of X-axis and Y-axis .....	20
3.6 Alignment of Air Cylinder .....	21

Figure	Page
3.7 Alignment of Spindle.....	21
3.8 Classification of Light Emission Levels: (a) Level 1, (b) Level 2, (c) Level 3 .....	23
3.9 Machined Surface for Level 2 Light Emission: (a) Test Number 2, (b) Test Number 5 ....	24
3.10 Machined Surface for Level 3 Light Emission: (a) Test Number 3, (b) Test Number 6 ...	24
3.11 Machined Surface Investigated by SEM (2000x Magnification). (a) At the Beginning of Machining with No Light Emission; (b) With Extensive Light Emission and Surface Melting .....	25
3.12 Machined Surface Investigated by SEM (8000x Magnification). (a) At the Beginning of Machining with No Light Emission; (b) With Extensive Light Emission and Surface Melting .....	26
3.13 Cross Section of Machined Surface: (a) Test Number 5, Level 2 Light Emission; (b) Test Number 6, Level 3 Light Emission .....	27
3.14 Diffraction Patterns of Machined Surface for (a) Original Surface (b) No Spark (c) Little Spark (d) Strong Spark with Melts at 60,000 rpm and 50,000 rpm .....	28
3.15 XRD of Chip and Machined Surface (Spindle Speed: 60,000 rpm, Feedrate: 3.0 $\mu\text{m}/\text{flute}$ )	30
3.16 EDS Patterns of (a) Original Surface (b) Machined Surface (c) Chip at Level 3 Light Emission.....	31
3.17 Crystallization Transition Curve.....	33
3.18 SEM Image of Tool Flank Face after Milling Process (a) BMG Material Adhere to the Flank Face (b) Build Up Edge .....	34
3.19 EDS Pattern of the Adhered Material .....	35
3.20 Comparison of New Tool and Worn Tool (a) New Tool (b) Worn Tool.....	35
3.21 Dry Machining Tool Wear for Different Spindle Speeds .....	35
3.22 Mist-coolant Machining Tool Wear for Different Spindle Speeds.....	36
3.23 Mist-coolant Machining Tool Wear Vs Dry Machining Tool Wear.....	37



Figure	Page
4.1 Schematic of Experimental System .....	40
4.2 Design Process for Vibration System .....	41
4.3 Working Graph of Actuator with Unipolar Operation at Different Voltage Levels .....	43
4.4 Vibration Stage (a) Basic Design (b) Thin-wall Structures .....	44
4.5 Design Process Flow Chart .....	46
4.6 Vibration Stage Boundary Condition.....	46
4.7 Desired Mode Shapes at (a) 8201 Hz (b) 8194 Hz .....	47
4.8 Displacement Sensor Probe Holder .....	50
4.9 Displacement from CutPro.....	50
4.10 Frequency Response Function of the Vibration Stage.....	51
4.11 Schematics of Micro-milling with Vibration Assistance in the (a) Normal and (b) Feed Directions .....	53
4.12 Tool Tip Trajectory with Respect to Workpiece with Vibration Assistance in the Normal Direction .....	54
4.13 Measure Surface Roughness .....	55
4.14 Surface Roughness with Vibration Amplitude. (Frequency: 8 kHz, Feedrate: 0.5 $\mu\text{m}/\text{tooth}$ , Radial depth of cut: 15 $\mu\text{m}$ ).....	57
4.15 Surface Roughness with Vibration Frequency (Amplitude: 1.2 $\mu\text{m}$ , Feedrate: 0.4 $\mu\text{m}/\text{tooth}$ , Radial depth of cut: 25 $\mu\text{m}$ ).....	58
4.16 Comparison of Surface Profile with and without Vibration Assistance .....	59

---

## CHAPTER I

### INTRODUCTION

#### 1.1. Background

Amorphous solids are defined as materials in which the atoms and the molecules are not arranged in a regular lattice pattern. Commonly used amorphous materials include glass, plastic, and bulk metallic glass (BMG), which have been widely used in various industrial areas such as optics, aerospace, sports, and biomedical applications. For example, silica based glass has high optical quality, high hardness, low cost, and is the most commonly used material in optical components. Figure 1.1 shows several applications of glass components processed by precision manufacturing in micro optics fabrication.

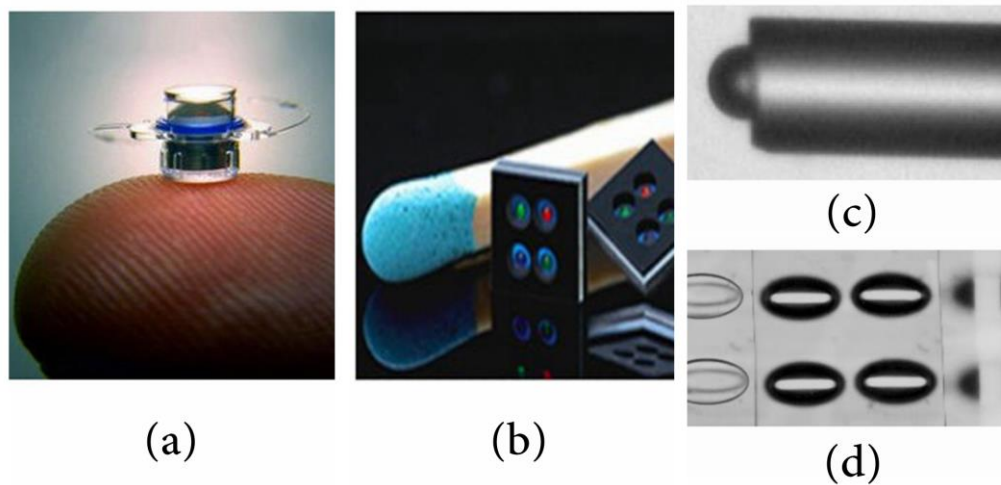


**Figure 1.1** Application of Micro-optics (a) Telescope (3.6 mm diameter and 4.4 mm length) [1] (b) Micro-camera (5.9 mm by 5.8 mm by 2.25 mm) [2] (c) Micro-lens (70  $\mu\text{m}$  diameter) [3] (d) Hemi-elliptical micro-lenses (284  $\mu\text{m}$  length) [3]

---

BMGs are a group of newly developed metallic materials with amorphous microstructure produced by rapid cooling of melted metal alloys [4]. Under a high cooling rate, the metal passes nucleation and crystalline phases during solidification, resulting in non-crystalline solid material. Compared to their crystalline counterparts, BMGs have superior mechanical properties, including higher hardness, improved corrosion resistance. BMGs have been increasingly used in optics, aerospace, sports, and biomedical applications, with the typical products shown in Figure 1.2.



**Figure 1.2** BMG Products (a) Golf Clubs [5] (b) Cellphone Case [6]

Geometric accuracy and surface quality are critical factors, which influence the functionality of BMG components. Precision machining techniques such as micro-turning, micro-milling, grinding and polishing need to be conducted in order to manufacture the parts with desired quality [7-10]. Micro-milling is capable of generating a high-slope freeform surface with micron-level geometric features. Compared to crystalline metallic materials, the fundamental mechanism of chip formation and surface generation in machining amorphous materials is different due to their unique microstructure and mechanical properties [11]. Furthermore, crystallization of BMGs microstructure may occur because of the stress and temperature variations in the material deformation zone, depending on the machining conditions [12].

Machining of silicate glass is also challenging, since glass is a brittle material with low fracture toughness and high hardness. In the machining of glass, fracture is the dominant material removal mode instead of plastic deformation for metallic materials [13]. The cutting forces cause crack generation on the

machined surface, which is detrimental to the quality of the optical parts. However, it has been demonstrated that when the uncut chip thickness is below a critical value, the material deformation goes through the brittle-ductile transition, and a crack free surface can be achieved.

Vibration assisted machining (VAM) is a proven process to be beneficial in the machining of brittle materials. In VAM, high frequency and small amplitude vibration is applied to either the tool or the workpiece in addition to the original cutting motion. VAM can be broadly classified into two types: 1-D and 2-D. In 1-D VAM, tool or workpiece is driven along or perpendicular to feed direction and results in a reciprocating motion, as shown in Figure 1.3-(a). 2-D VAM has vibrations along both directions, thus resulting in a circular or elliptical movement between tool and workpiece, as shown in Figure 1.3-(b). The added vibration changes the fundamental mechanism of chip formation and surface generation in the machining process [14-17]. Compared to conventional machining, VAM has the advantages of increasing tool life, improving surface roughness, and reducing cutting force etc. [18-23].

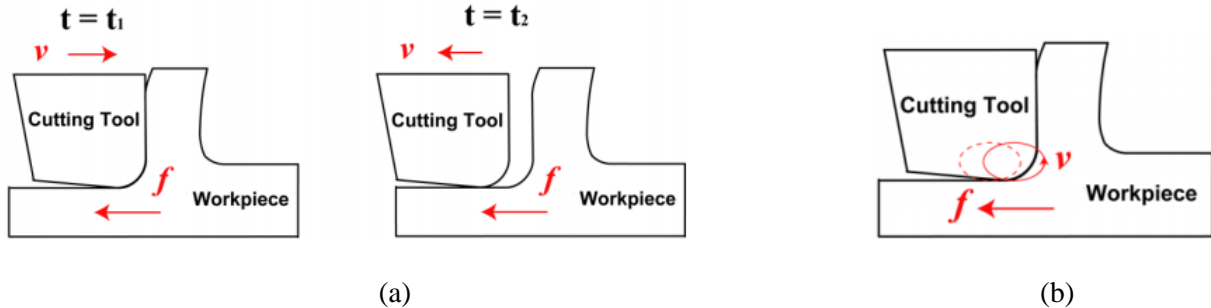


**Figure 1.3** Comparison of 1-D and 2-D Vibration (a) 1-D (b) 2-D [24]

## 1.2. Objective and Approach

The objective of this thesis is to investigate the machinability in the micro-milling of amorphous Zr-BMG and BK-7 optical glass. A three-axis precision micro-milling machine is developed to conduct the machining experiments. Light emission and surface microstructure in the micro-milling of Zr-BMG is studied to determine the effect of milling conditions on the surface quality. The effect of coolant on progressive tool flank wear in the micro-milling of Zr-BMG is investigated. In the micro-milling of BK-7

---

optical glass, a vibration stage is developed to achieve 2-D vibration assistance in the machining process. The vibration stage has a thin-wall design and it is driven by piezo actuators. The dynamic behavior of the vibration stage is calibrated. The effects of vibration direction, amplitude and frequency on the machined surface quality of BK-7 glass are determined. The outcome of this research is to experimentally evaluate the machinability in the micro-milling of typical amorphous materials including Zr-BMG and BK-7 optical glass. The results are able to provide optimum machining conditions to achieve high machining efficiency and high component quality.

---

## CHAPTER II

### LITERATURE REVIEW

In this chapter, previous studies on the machining of BMG and optical glass are reviewed. The VAM technology for amorphous materials is discussed. The state-of-art technology and possible improvements based on the literature survey and the motivation for this study are introduced.

#### **2.1. Machining of Bulk Metallic Glass**

It is well known that most metals are crystalline because the crystallization occurs when the materials are cooled from a liquid state. However, if the cooling rate exceeds a critical value, there is not enough time for crystallization and results in solid material with amorphous microstructure, as in the case of BMG. The unique microstructure of BMG is responsible for major differences in mechanical behaviors compared to crystalline materials [4,11,25].

Machining of BMG is required to achieve complex geometry with high accuracy and low surface roughness. In the machining process, the mechanical properties and microstructure of BMGs are affected by machining temperature and stress variation [4]. Therefore, it is necessary to investigate the machinability of BMG to improve efficiency and component quality. Bakkal et al. [11] performed experimental investigations in the turning of Zr-based BMG at various cutting speeds, tool rake angles and coating properties. It was found that the occurrence of light emission in the turning process was related to the melting of BMG chips. High cutting speed significantly reduced the forces due to thermal softening effect. Surface roughness in the turning of BMG was better than those of Al6061 and SS304. Fast tool wear and edge chipping were found during short machining time. X-Ray diffraction (XRD) and Scanning Electron

---

Microscopy (SEM) results showed crystallization of machined chips at high cutting speed in Figures 2.1 and 2.2, while no crystallization occurred on the machined surface. XRD peaks matched the pattern of monoclinic ZrO<sub>2</sub>, confirming that oxidation was associated with light emission and high flash temperature during the turning process [12]. The chip morphology showed the presence of shear bands, void formation, and enhanced viscous flow at higher cutting speed [26]. Crystalline grain, residual amorphous region, and phase separation were observed in the amorphous–crystalline transition region of machined chips by Transmission Electron Microscope (TEM) examinations [27]. Jiang and Dai [28] performed the turning experiments on Zr-based BMG, and concluded that the formation of lamellar chips was due to repeated shear-band formation in the primary shear zone (PSZ). A coupled thermomechanical orthogonal cutting model considering force, free volume and energy balance in the PSZ was developed to quantitatively characterize the lamellar chip formation.

Bakkal et al. [29] performed drilling on Zr-based BMG with HSS and WC–Co tools. It was observed that holes with good surface finish could be produced when spindle speed was below the critical value causing the light emission of the chip. However, some large size burr formations at the edge of the holes were identified, and a new type of chip with long tangled ribbon shape was observed. Thrust force, torque, and tool wear were determined for the drilling of BMG with different tool materials and cutting conditions [30].

An experimental study on the grinding of Zr-based BMG was conducted by Bakkal et al [31]. It was found that grinding forces reduced with the increasing of cutting speed as specific grinding energy increased. The machined surface and chip morphology showed that material removal and surface formation of BMG were mainly due to the ductile chip formation and ploughing as well as brittle fracture of some particles from the edge of the tracks. A conventional Al<sub>2</sub>O<sub>3</sub> wheel was not suitable for grinding of the BMG in dry conditions due to extensive light emission.

Bakkal and Naksiler [32] further conducted investigations on the end-milling of Zr-based BMG. The effects of feedrate on cutting force, burr formation, and surface roughness were determined with a

constant spindle speed of 5000 rpm. It was found that BMG required less cutting forces compared to SS304, and higher forces than Al6061 under the same cutting conditions. The burr rollover and the top burr formations were observed along the milling slot. Furthermore, cutting forces and burr formations were characterized in spiral and slot milling paths [33].

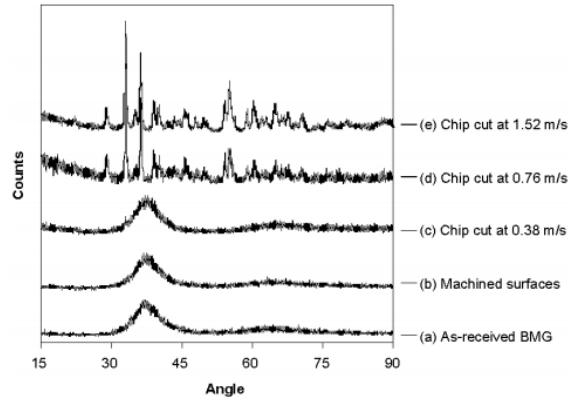


**Figure 2.1** X-ray Diffraction Result for As-received, Machined Surface and Chips [11]

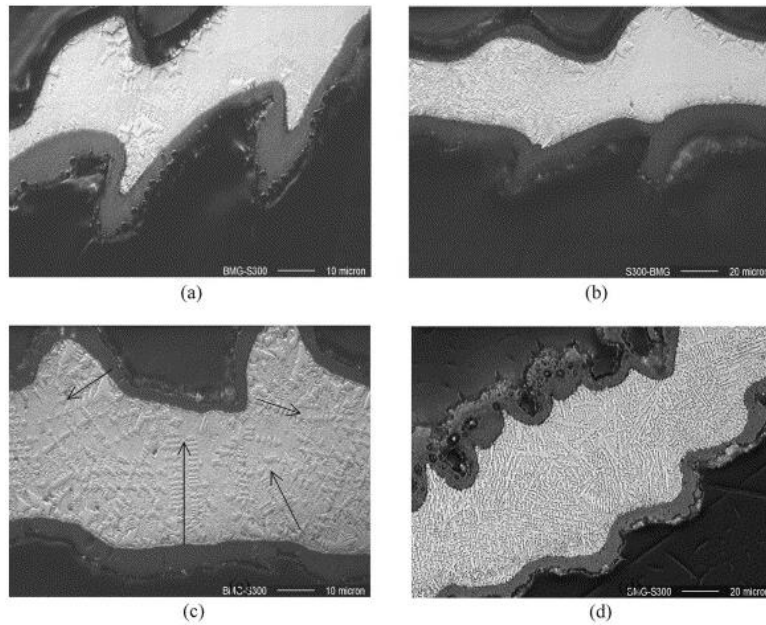


**Figure 2.2** Optical Micrographs of Cross-Section of Chip (a) Crystallization Incipient near the Oxide Layer, (b) Transition From Crystalline (Left) to Amorphous (Right) Regions, (c) Dendritic Crystalline Branch and the Maximum Cooling Rate Directions Indicated by Arrows, (d) Fully Crystalline Region

[11]



## 2.2. Machining of Optical Glass

Machining of optical glass is required to produce optical components with desired geometric accuracy and surface quality. It is challenging to achieve satisfactory surface quality in machining optical glass due to its brittleness and hardness. Conventional machining causes a fractured surface and requires additional finishing processes, which are expensive and time consuming [34]. However, when the depth of cut is below a critical value, defined as critical depth of cut, the brittle glass material can be machined in ductile mode, which was first reported by King and Tabor [35]. Ductile-mode machining is necessary to achieve satisfactory machining performance.

A lot of studies have been conducted to investigate the factors that influence the critical depth of cut. Blackely and Scattergood [36] developed a model for turning of brittle material to achieve ductile machining, as shown in Figure 2.3.  $y_c$  represents the average fracture propagation depth. If the damage does not go beyond the cut surface plane, ductile-mode machining is obtained. It was found that rake angle has major effect on critical depth of cut. A negative rake angle is inclined to achieve ductile-mode machining.

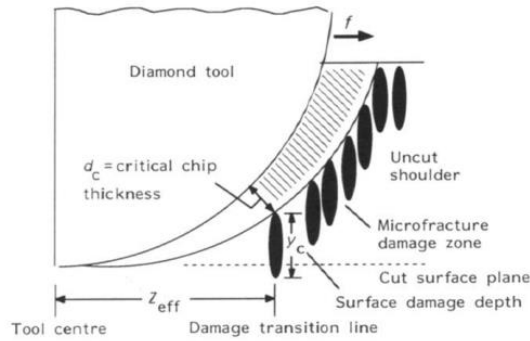


**Figure 2.3** Machining Geometry Used to Derive the Cutting Model [36]

Critical depth of cut varies for different materials depending on the material property. Bifano et al. [31] described a function to represent critical depth of cut ( $d_c$ ) for grinding in terms of fracture toughness ( $K_C$ ), hardness ( $H$ ) and modulus of elasticity ( $E$ ) as:

$$d_c \propto \left(\frac{E}{H}\right) \left(\frac{K_C}{H}\right)^2$$

---

Unlike turning and grinding, studies on the milling of brittle material are relatively limited. Muhammad A. et al. experimentally investigated the ductile-mode machining of glass in the milling process [37, 38]. It was demonstrated that the fracture-free surface could be achieved under certain cutting conditions. It was also reported that ductile-mode milling in glass is sensitive to feedrate and radial depth of cut when the feedrate is low. However, if feedrate exceeds a critical value, the ductile machining becomes insensitive to radial depth of cut. Furthermore, a physical model was developed to evaluate the effect of tool diameter on critical feedrate [39], and it was concluded that larger diameter significantly increased the critical feedrate.

### **2.3. Vibration Assisted Machining for Brittle Materials**

#### *2.3.1. Vibration Assisted Machining System*

In the conventional machining of brittle materials, the critical depth of cut is normally at a sub-micron level. A great deal of research has been conducted to achieve higher depth of cut for ductile-mode machining to increase the productivity. It has been demonstrated that the application of vibration assistance in the machining of brittle materials is beneficial. Vibration assisted machining (VAM) introduces high frequency vibration between the tool and the workpiece through external actuators. Based on the motion of tool tip, VAM can be classified into two types: 1-D VAM and 2-D VAM. As 1-D VAM has a relatively simple geometry, it has been widely used in previous research [40-42]. Figure 2.4-(a) illustrates the vibration motion of 1-D VAM. It is found that tool tip moves in a reciprocating trajectory and the contact between rake face the uncut materials depends on the vibration frequency and the amplitude, with the position  $x(t)$  and velocity  $x'(t)$  expressed as:

$$x(t) = A \times \sin(2\pi ft) + Vt \quad (1)$$

$$x'(t) = 2\pi fA \times \cos(2\pi ft) + V \quad (2)$$

where  $A$  and  $f$  are the amplitude and frequency of vibration,  $V$  is feed speed. Eq. (2) defined a critical feed speed  $V_c = 2\pi fA$ . If  $V < V_c$ , the tool-workpiece contact becomes intermittent at the frequency of  $f$ , which is desired for most cases. If  $V > V_c$ , the cutting is continuous as conventional machining.

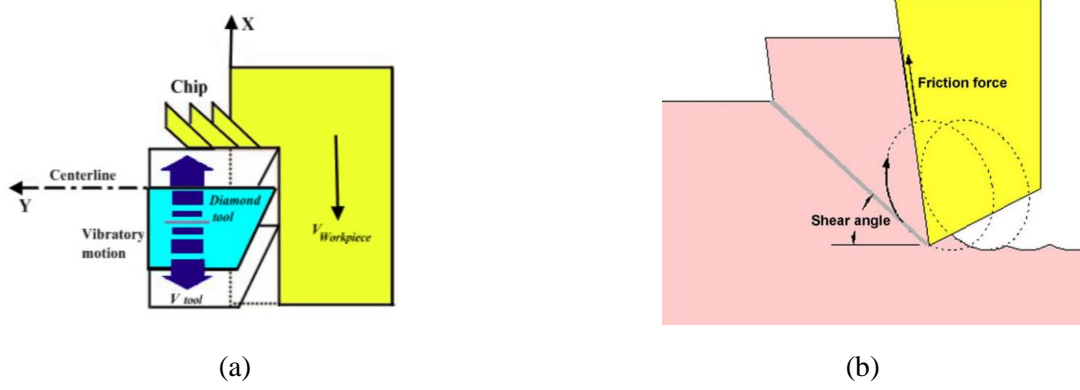


**Figure 2.4** Vibration Motion of (a) 1-D VAM [43] (b) 2-D VAM [44]

2-D vibration is also known as elliptical vibration as it adds vibration to the vertical motion as well as to the horizontal motion, which results in elliptical or circular motion of tool tip. Figure 2.4-(b) provides the kinematics of 2-D VAM. The position  $x(t)$ ,  $y(t)$  and velocity  $x'(t)$ ,  $y'(t)$  can be expressed as:

$$x(t) = A \times \sin(2\pi ft) + Vt \quad (3)$$

$$y(t) = A \times \cos(2\pi ft) \quad (4)$$

$$x'(t) = 2\pi fA \times \cos(2\pi ft) + V \quad (5)$$

$$y'(t) = -2\pi fA \times \sin(2\pi ft) \quad (6)$$

A typical 1-D VAM system is shown in Figure 2.5-(a). An ultrasonic generator converts electric signals to reciprocating vibration motion, then are amplified by the sonotrode due to resonance, which is finally translated to the tool attached to the end of sonotrode. The frequency of 1-D resonant system varies from 20 kHz to 40 kHz, and the amplitude varies from 3  $\mu\text{m}$  to 100  $\mu\text{m}$  [44-46]. 2-D resonant system uses the same driving mechanism as 1-D VAM, but the tool tip moves in a circular or elliptical trajectory. Moriwaki and Shamoto [47] developed a structure shown in Figure 2.5-(b). Two piezo actuators are

attached to the surface of a beam structure. The piezo actuators are driven at the structure's natural frequency, but with different phases. The bending mode of the structure is excited, resulting in an elliptical path at the tool tip.

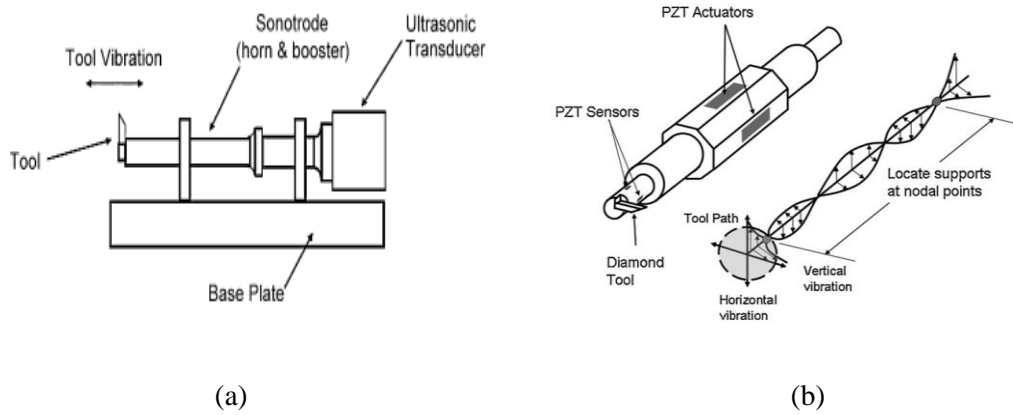


**Figure 2.5** VAM System (a) 1-D [43] (b) 2-D [46]

### 2.3.2. Benefits of VAM for brittle materials

It has been reported that using VAM to machine brittle materials offers a multitude of benefits, such as a smaller cutting force, longer tool life, higher critical depth of cut, improved finished surface etc. Zhou et al. [48] performed the vibration assisted groove cutting, and found that the cutting force decreased due to the dynamic friction and higher lubrication efficiency of the cutting fluid derived from the periodic separation between tool and workpiece. Ishikawa et al. [49] conducted a series of experiments in the drilling of ceramics with the assistance of ultrasonic and low frequency vibration. The drilling force decreased up to 70% by increasing vibration amplitude, as compared to conventional drilling. Egashira & Mizutani [50] obtained the same results in the ultrasonic micro-drilling of glass.

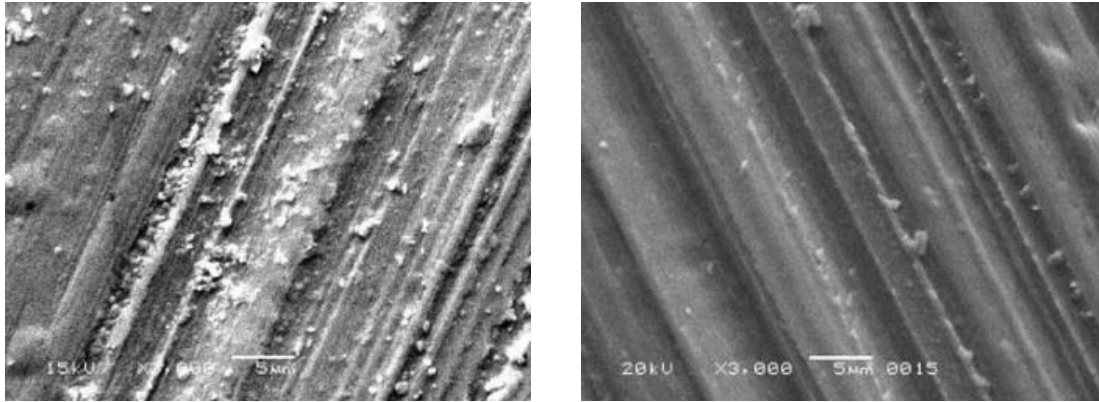
Tool life is extended in VAM due to the smaller cutting force compared to conventional machining. Moreover, the periodic separation between the tool and the workpiece is also helpful to release the stress of the tool and consequently results in longer tool life. Suzuki et al. [51] observed a remarkable reduction of tool wear in the 2-D ultrasonic VAM of Tungsten Alloy. Gong et al. [52] investigated the effect of ultrasonic vibration on tool wear in the grinding of K9 glass. The kinematics of the grinding tool with

---

vibration assistance was investigated. It showed that less simultaneous depth of cut is the main reason that the tool wear rate is less. Duty cycle, defined as the fraction of cutting time in one vibration cycle, is also a major factor in influencing tool life. It was proposed by Rubenach [53] that the tool wear rate at 10% duty cycle with 75m cutting distance is only one-third of the wear rate at 40% duty cycle with 450m cutting distance in glass machining.

It has been claimed that VAM can increase the critical depth of cut in the ductile machining of brittle materials. Moriwaki et al. [17] carried out a turning test on soda-lime glass with 1-D ultrasonic vibration. The critical depth of cut increased from 0.03 $\mu\text{m}$  in conventional turning to 0.4  $\mu\text{m}$  in VAM. Zhou et al. [48] obtained the similar result from groove cutting experiments. 2-D VAM on other brittle materials such as Tungsten Carbide, Zirconia Ceramics, Calcium Fluoride and glass has been conducted by SUZUKI et al. [54]. The results show that the critical depth of cut for all of these brittle materials increased significantly in 2D-VAM.

The improvement of machined surfaces in 2-D VAM of Nano  $\text{ZrO}_2$  has been investigated by Yan et al. [55]. The machined surface in conventional diamond grinding and 2-D ultrasonic assisted grinding with the same cutting condition are compared, as shown in Figure 2.6. Results indicate that the 2-D ultrasonic vibration improved the surface quality effectively. There are two reasons for this phenomenon. Firstly, the abrasive particles with high-frequency vibration have a polished effect, generating a smooth surface. Secondly, VAM reduced tool wear and cutting force, therefore improving the quality of the machined surface.



(a)

(b)

**Figure 2.6** SEM Photographs of Mano-ZrO<sub>2</sub> after (a) Conventional Diamond Grinding (b) 2-D Ultrasonic Assisted Grinding [48]

#### 2.4. Summary

The unique microstructure and mechanical properties of BMGs bring new challenges in precision machining processes. It is found from the literature that machining of BMG is mainly focused on the turning and drilling processes, and the effect of coolant on machining BMG has not been investigated. Thus, an investigation of machinability in milling is necessary for manufacturing BMG components with complex geometry.

Glass materials are widely used as lens for optical components. Ductile-mode machining is required to achieve a crack-free surface. It has been demonstrated that vibration assistance improves the critical chip thickness corresponding to ductile machining. However, the effects of the direction, frequency and amplitude of vibration on machining performance is not clear, which inhibits the application of VAM in machining glass materials.

In this thesis, experiments are conducted base on micro-milling of Zr-BMG and BK-7 glass materials. In the machining of Zr-BMG, the surface quality is analyzed through SEM and metalloscope. XRD is conducted to investigate the effect of cutting parameters on surface crystallization. Tool flank wear with respect to spindle speeds in both dry and mist-coolant micro-milling of Zr-BMG is measured.

---

Furthermore, experimental investigations on the fundamental mechanisms of surface generation in vibration assisted micro-milling of glass are conducted. Contrary to the vibration assisted turning process presented in the literature, the milling process involves varying uncut chip thickness due to the rotation of the milling tool. A two-dimensional vibration stage with adjustable amplitude and frequency is developed. The effects of the direction, amplitude and frequency of vibration on the surface roughness and damage are investigated.

---

## CHAPTER III

### MACHINABILITY IN THE MICRO-MILLING OF ZIRCONIUM BASED BULK METALLIC GLASS

#### **3.1. Overview**

The objective of this chapter is to investigate the machinability of BMGs in the micro-milling process. A high-speed micro-milling machine was developed to perform the experiments. The effect of cutting parameters on light emission in micro-milling is discussed. The microstructure of the machined surface was characterized using SEM, XRD, Energy Dispersive Spectroscopy (EDS) and metalloscope. Cutting parameters corresponding to the onset of the crystallization transition of the machined surface were determined. The effect of mist-coolant on progressive tool flank wear with respect to cutting speeds was investigated. The results of this study provide the cutting conditions to improve the surface quality and reduce the tool wear.

#### **3.2. Experimental Setup**

##### *3.2.1. Description of the experimental setup*

The milling experiments on Zr-based BMG were conducted with spindle speeds from 10,000 to 105,000 rpm. Two micro-milling machines with different spindle speed range capacities were used, including a commercial MDA precision micro-milling machine (Figure 3.1 (a)) with a spindle speed in the range of 10,000 - 60,000 rpm, and an in-house developed high-speed micro-milling machine at 60,000 - 160,000 rpm (Figure 3.1 (b)). A two-flute AlTiN coated end mill (MICROCUT) with 3.175 mm diameter and 30° helix angle was used. The workpiece was Zr-based BMG (model: LM105) provided by Liquidmetal



Technologies Inc. The composition and the mechanical properties of the BMG workpiece are listed in Tables 3.1 and 3.2 respectively. The dimension of the workpiece was 21 mm × 14 mm × 2 mm.

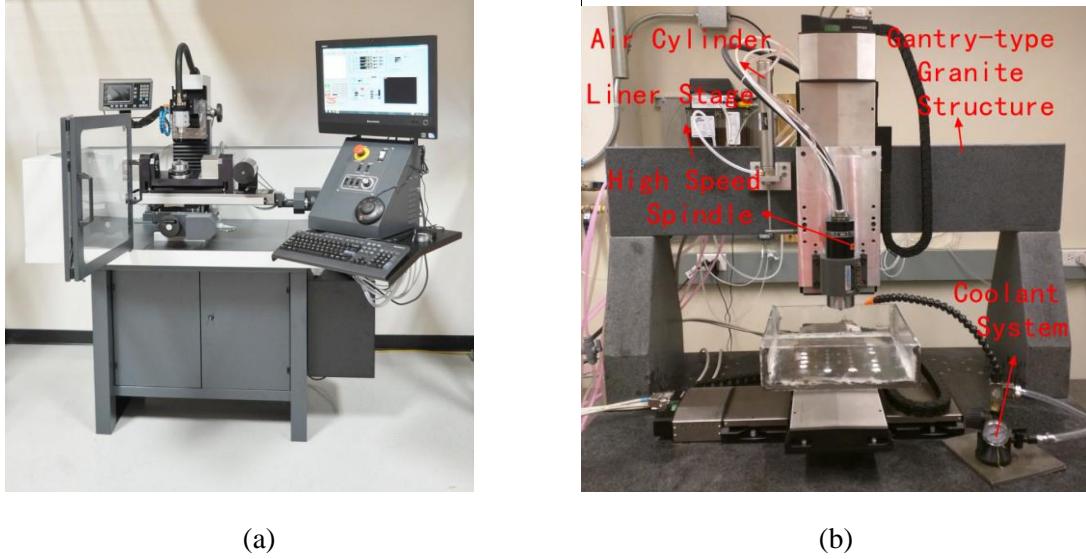


**Figure 3.1** (a) MDA Precision Micro-Machining Center (b) High Spindle Speed Machining System

**Table 3.1** Composition of LM105 Bulk Metallic Glass [56]

	Zr	Ti	Cu	Ni	Al
at%	52.5	5	17.9	14.6	10
wt.%	65.7	3.3	15.6	11.7	13.7

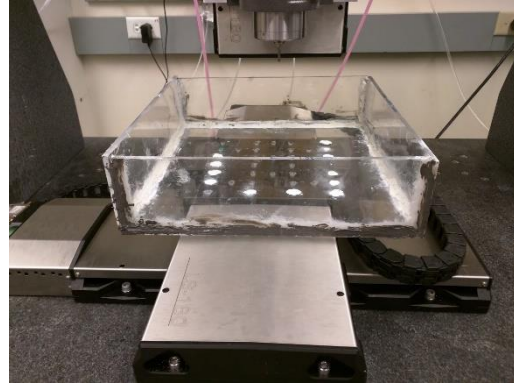
**Table 3.2** Mechanical Properties of LM105 Bulk Metallic Glass [56]

Density (g/cm <sup>3</sup> )	Hardness (HRC)	Yield Strength (MPa)	Young's modulus (GPa)	Fracture toughness (MPa√m)	Poisson's ratio	Glass transition temperature (°C)	Crystallization temperature (°C)
6.57	53	1524	92.7	~40	0.38	399	468

A mist-coolant dispenser shown in Figure 3.2-(a) was used, the coolant which was semi-synthetic 380, mixed with water in the proportion of 1:20. The flow rate was 126 ml/min. To protect the linear stage from coolant, a sink was used to collect the coolant as shown in Figure 3.2-(b).



(a)



(b)

**Figure 3.2** Coolant System (a) Dispenser (b) Sink

### 3.2.2. Development of high spindle speed micro-milling machine

A high speed micro-milling system was developed with the structure shown in Figure 3.1 (b). It was composed of five components: gantry-type granite structure, linear stages, high speed spindle, coolant system and air cylinder. Granite was used for the machine structure to ensure high rigidity and reduce the thermal effect of the environment. Three LS-180 linear stages with a 50 nm resolution from Physik Instrument (PI) were assembled to achieve the feed motions in three axes. An angular-contact bearing spindle SC 1060-OA with a speed range of 60,000 – 160,000 rpm from Fischer Precise was mounted on the Z-axis linear stage. An air cylinder was used to counterbalance the weight of the spindle and spindle holder. The specifications of the linear stage and high speed spindle are given in Tables 3.3 and 3.4. The schematic of the whole system is shown in Figure 3.3.

**Table 3.3** Specification of Linear Stage [57]

LS-180 Liner Stage					
Travel Range (mm)	Maximum Speed (mm/sec)	Straightness ( $\mu\text{m}$ )	Pitch ( $\mu\text{rad}$ )	Yaw ( $\mu\text{rad}$ )	Resolution (nm)
155	200	$\pm 2$	$\pm 40$	$\pm 50$	20
FX (N)	FY (N)	FZ (N)	MX (Nm)	MY (Nm)	MZ (Nm)
500	200	1000	132	400	125

---

**Table 3.4** Specification of Spindle [58]

SC 1060-OA Spindle				
Speed Range (rpm)	Torque (S1- 100%) (N-m)	Bearings Type	Lubrication	Runout Accuracy ( $\mu\text{m}$ )
6000-16000	0.03	Angular-contact	Oil-air	$\leq 2$
Balance Quality (mm/sec)	Radial Shaft Stiffness (N/ $\mu\text{m}$ )	Axial Shaft Stiffness (N/ $\mu\text{m}$ )	Cooling	Tool Diameter (mm)
$\leq 1$	25	17	Liquid Circulation	3.175

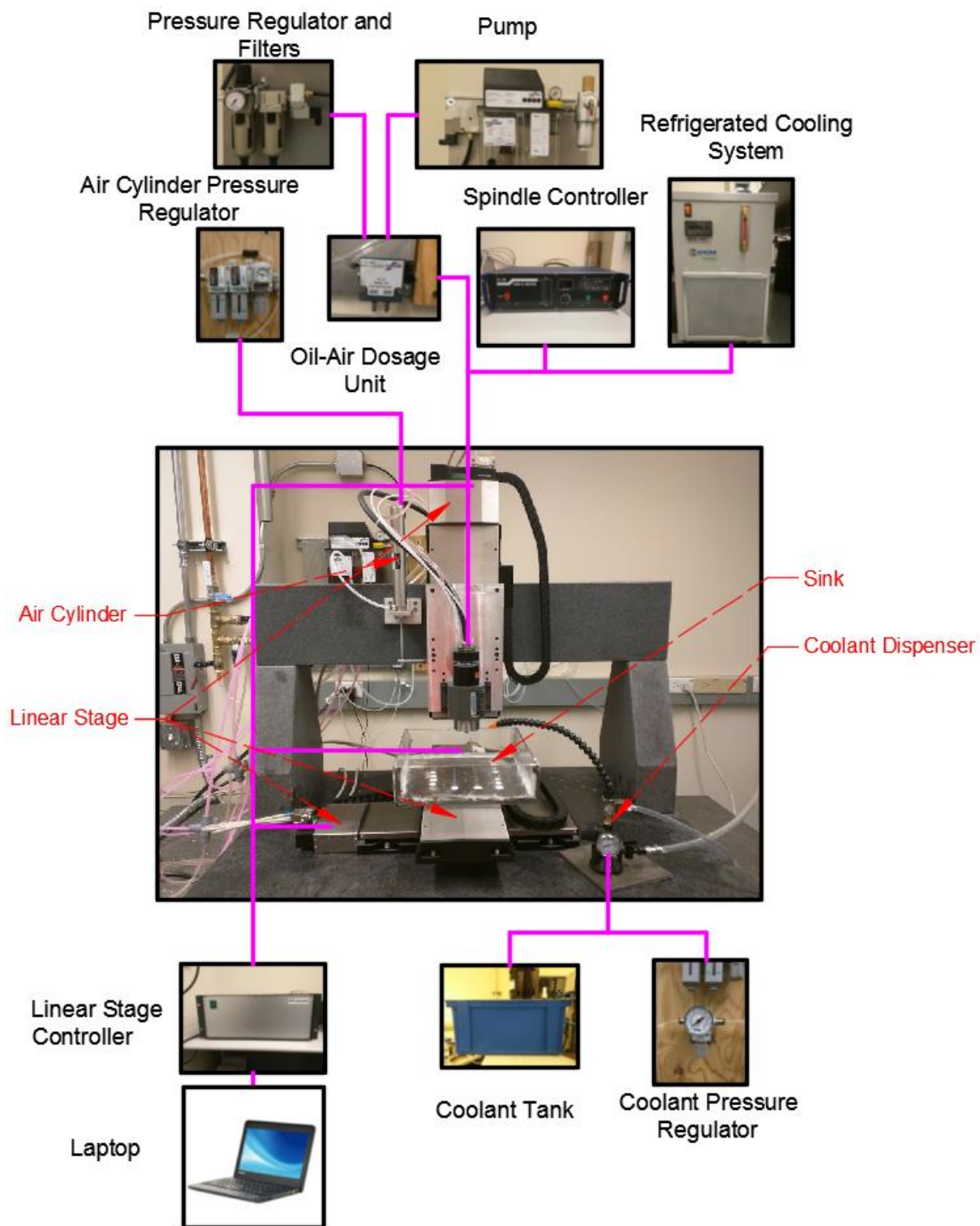


**Figure 3.3** Schematic of High Speed Machining System

---

It is important to calibrate the perpendicularity in assembling the three linear stages and the spindle. The calibration process is described as follows:

1. Alignment of the Z-axis: Fix a precision dial indicator with a resolution of 0.001 inch on the Z-axis. The probe of the dial indicator touches the side of the rectangular block, which is aligned at  $90^\circ \pm 5'$  with respect to granite stage. Adjust the orientation of the z-axis to make sure that the variation of the dial indicator reading along the whole movement range is less than 0.001 inch. The alignment setup is shown in Figure 3.4.



**Figure 3.4** Alignment of Z-axis

2. Alignment of X-Y stages: Place two precision rectangular blocks that are aligned  $90^\circ \pm 5'$  with respect to each other on the granite stage. Use the dial indicator to adjust the X-axis linear stage based on one of the rectangular block. Make sure the variation of dial indicator reading along the whole movement range of the X-axis is less than 0.001 inch. Then use the dial indicator to adjust the Y-axis linear stage based on the other rectangular block. Make sure the variation along the whole movement range is less than 0.001 inch. The alignment setup is shown in Figure 3.5.

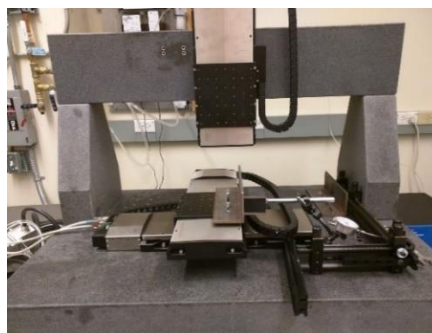


**Figure 3.5** Alignment of X-axis and Y-axis

- 
3. Alignment of air cylinder: Fix the air cylinder holder on the granite structure; then use level indicator to make sure it is parallel to the Y-axis linear stage, as shown in Figure 3.6 (a). Install the air cylinder and spindle, adjust the pressure of cylinder until it just balances the weight of the spindle and the spindle holder, as shown in Figure 3.6 (b).

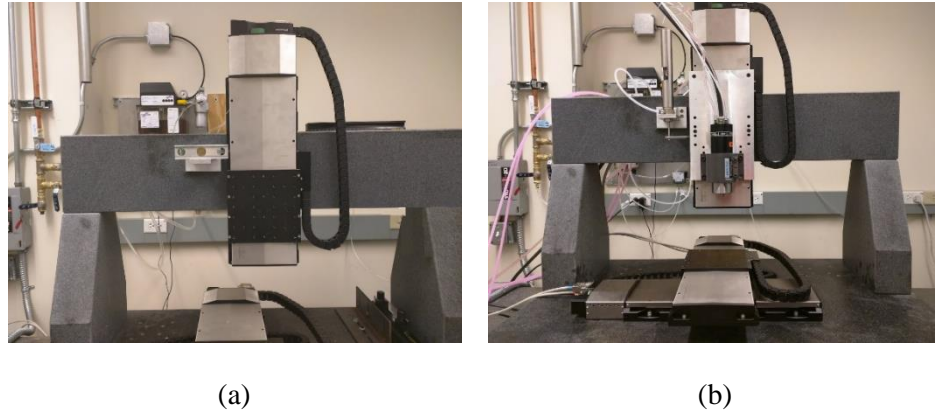


**Figure 3.6** Alignment of Air Cylinder

4. Alignment of spindle: Clamp one side of an L-shape bar onto the spindle; then connect the other side with dial indicator so that the dial indicator will rotate with spindle. In order to guarantee the perpendicularity between the cutting tool and the X-Y stage, the spindle needs to be realigned. The procedure is: Loose three out of the four screws that fix the spindle onto Z-axis, rotate the spindle and adjust it until the variation of dial indicator reading in one rotation is less than 0.0005 inch. The alignment setup is shown in Figure 3.7.

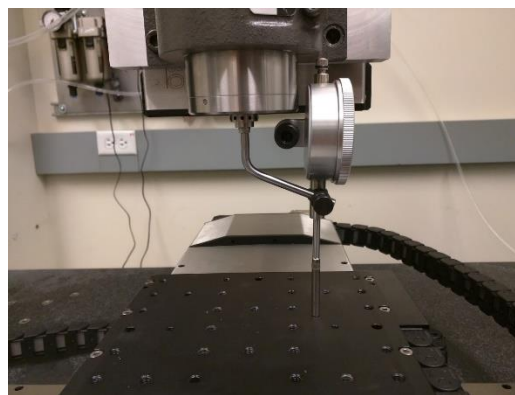


**Figure 3.7** Alignment of Spindle

---

### 3.3. Experimental Process of Micro-milling of Zr-BMG

Side milling of the BMG workpiece was conducted with an axial depth of cut of 2 mm. Two small radial depth of cut of 0.2 mm and 0.44 mm were selected due to fast tool wear rate and edge chipping at larger depth. The feedrate value ranged from 0.5  $\mu\text{m}/\text{flute}$  to 10  $\mu\text{m}/\text{flute}$ . Higher radial depth of cut or feedrate led to complete tool wear in one cutting path. Hitachi S-4800 scan electron microscope and Zeiss Observer.Z1m metalloscope were used to determine the morphology and microstructure of the machined surface. The cross section of the surface was finely polished for the examination purpose. Bruker AXS D8 Discover X-ray diffractometer was used to investigate the surface crystallization due to the milling process. EDS was used to determine the constituent elements of machined chip and surface. At each spindle speed, different values of feedrate were tested in order to determine the milling conditions that correspond to the onset of surface crystallization. An optical microscope was used to determine the width of tool flank wear with respect to the machining distance. Tool wear was compared for the milling process with and without the application of mist coolant at various spindle speeds.

#### 3.3.1. *Light emission in the micro-milling process*

Light emission was observed in the experiment process. The occurrence and strength of the light emission depended on the machining conditions. Table 3.5 shows the cutting parameters and the results of light emission strength, which are classified into three levels, explained below:

(1) No light emission was generated during the whole milling process, shown as Figure 3.8 (a), and defined as level 1;

(2) There was no light emission at the beginning of the milling process, however, intermittent light appeared in the later stage of the process due to heat accumulation in the material removal region, shown in Figure 3.8 (b) and defined as level 2;

(3) Strong light emission started to develop after about 3-5 seconds of milling process, shown as Figure 3.8 (c). Associated with the light generation, workpiece material was melted and deposited on the machined surface. This light emission strength is defined as level 3.

**Table 3.5** Light Emission Level in Different Experiments

Test Number	Spindle Speed (rpm)	Feedrate ( $\mu\text{m}/\text{flute}$ )	Light Emission Level
1	50,000	0.5	Level 1
2	50,000	3	Level 2
3	50,000	4.5	Level 3
4	60,000	0.5	Level 1
5	60,000	1	Level 2
6	60,000	3	Level 3

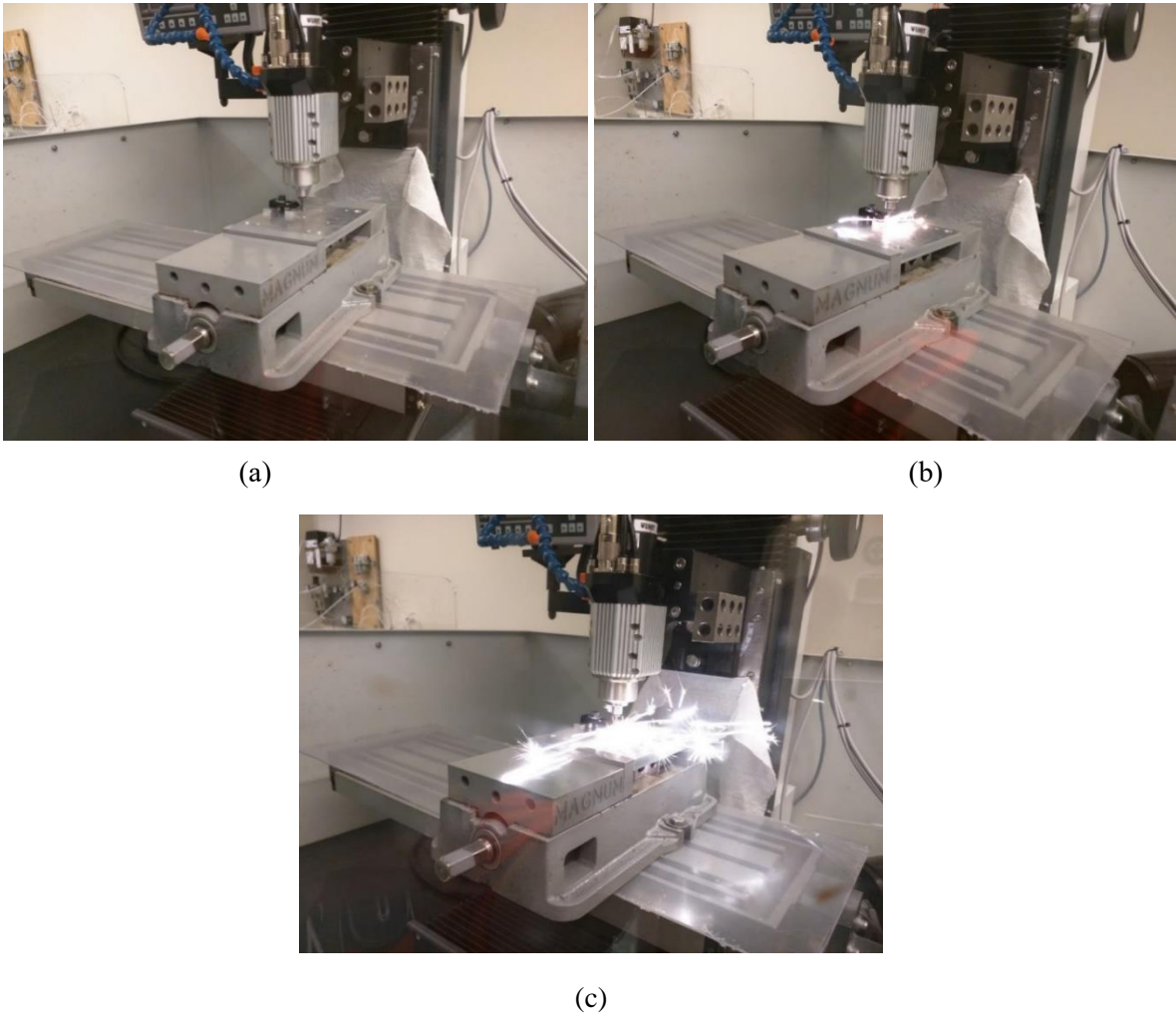


**Figure 3.8** Classification of Light Emission Levels: (a) Level 1, (b) Level 2, (c) Level 3



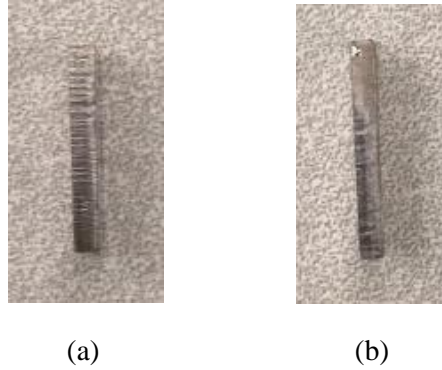


**Figure 3.9** Machined Surface for Level 2 Light Emission: (a) Test Number 2, (b) Test Number 5

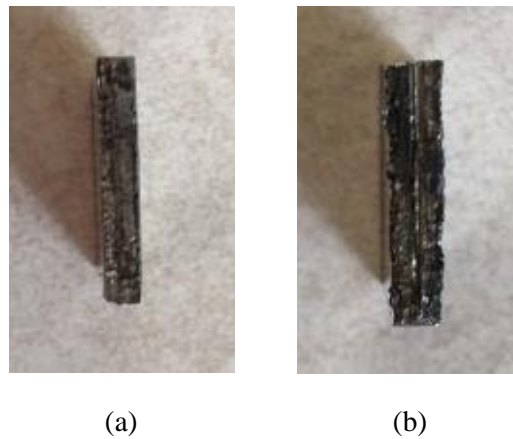


**Figure 3.10** Machined Surface for Level 3 Light Emission: (a) Test Number 3, (b) Test Number 6

The results in Table 3.5 show that the strength of light emission increases with feedrate at constant spindle speed, and the increase of spindle speed enhances the generation of light emission. This is due to higher stress and temperature when spindle speed and feedrate increase. Figure 3.9 and 3.10 show the pictures of machined surface corresponding to the tests listed in Table 3.5. Figure 3.9 (a) and (b) are based on the process with level-2 light emission. It is found that there is no significant change in the machined surface morphology between the regions with and without light emission. On the other hand, for Figures 3.10 (a) and (b), which correspond to level-3 light emission, the machined surface involved with melting of workpiece material turns into black color, and the surface roughness is higher compared with the surface in levels 1 and 2. Therefore, it is proved that the melting of surface material is detrimental to the surface quality in the milling process, while light emission itself is not directly related to the surface morphology.

---

### 3.3.2. Characterization of machined surface by SEM and metalloscope

The machined surface in the micro-milling of Zr-based BMG was investigated by SEM and metalloscope. Figure 3.11 shows the SEM images (2000x magnification) of machined surface under test number 3 (Table 3.5) with level 3 of light emission. Figure 4 (a) shows the machined surface at the beginning stage of the milling process when light emission is not generated. Figure 4 (b) shows the machined surface when extensive light emission is developed and melted material is deposited on the surface. Figure 3.12 shows the SEM results at the same location as Figure 3.11, and with higher magnification (8000x). It is found that the surface melting causes uneven surface morphology compared to the location with no light emission region, and results in solidified grain clusters at the size of 1-3  $\mu\text{m}$ .

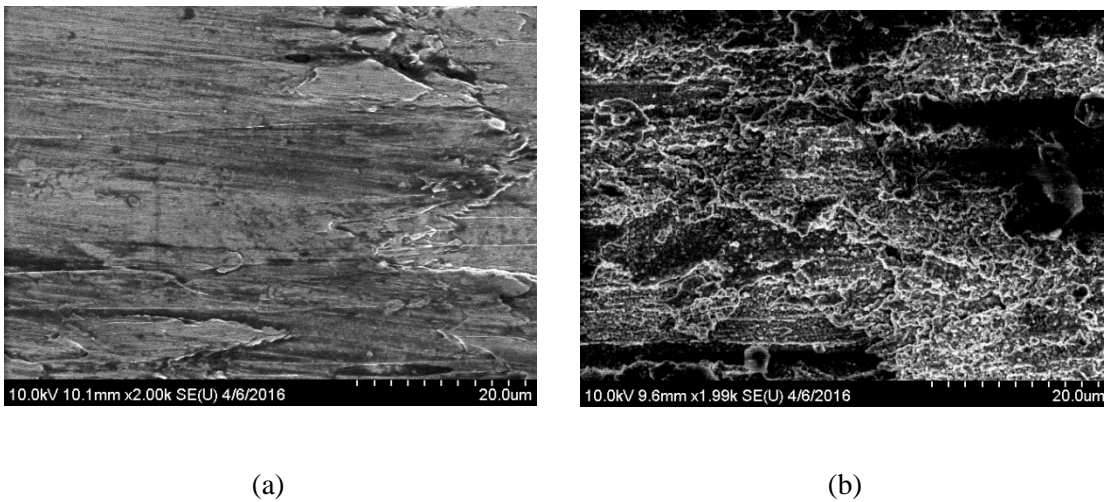
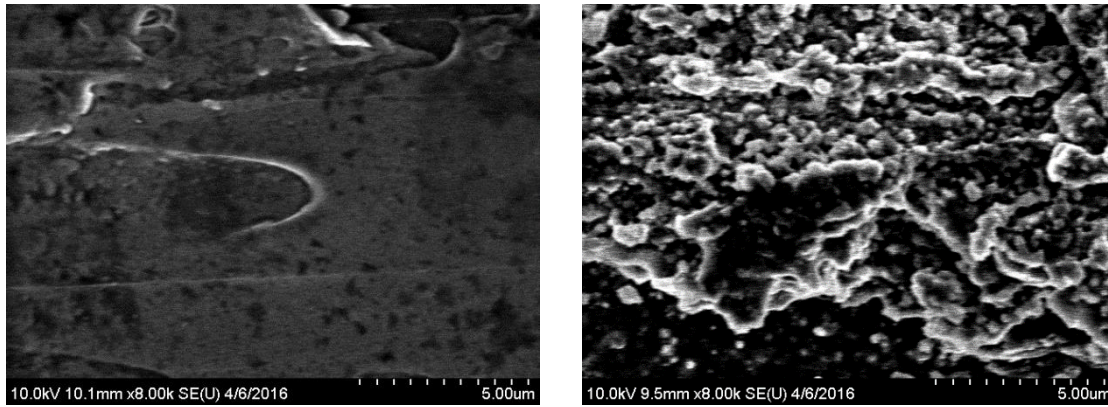


**Figure 3.11** Machined Surface Investigated by SEM (2000x Magnification). (a) At the Beginning of Machining with No Light Emission; (b) With Extensive Light Emission and Surface Melting

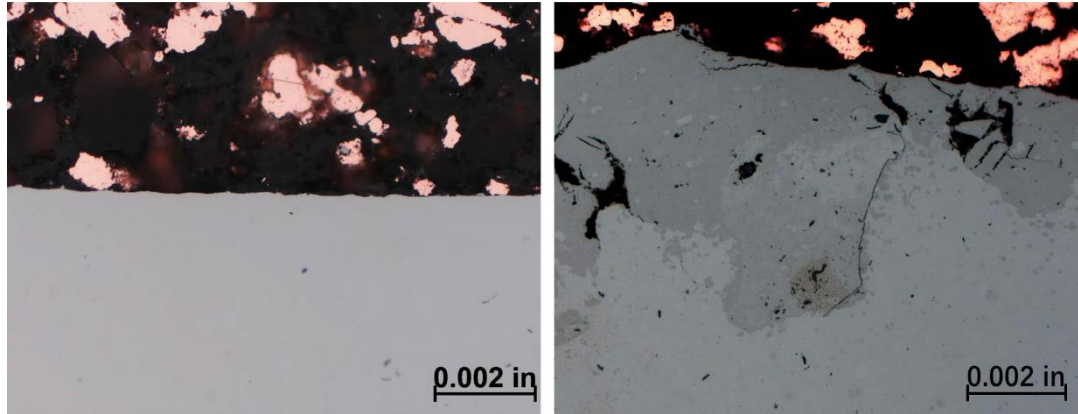


(a)

(b)

**Figure 3.12** Machined Surface Investigated by SEM (8000x Magnification). (a) At the Beginning of Machining with No Light Emission; (b) With Extensive Light Emission and Surface Melting

The cross sections of the machined surfaces were further examined by metalloscope in order to investigate the microstructure property. The workpieces were cut into half and the cross sections were finely polished for the examination. Figure 3.13 (a) and (b) show the cross sections of machined surfaces at the light emission levels of 2 and 3 when the spindle speed is 60,000 rpm, corresponding to test number 5 and 6 given in Table 3.5. The surface cracks and voids are visible in Figure 3.13 (b), but not in Figure 3.13 (a). When the feedrate increases, the temperature is high, which results in the melting of the material. The voids formation is due to the dynamic solidification process, which may cause degradation of the mechanical properties of machined components.



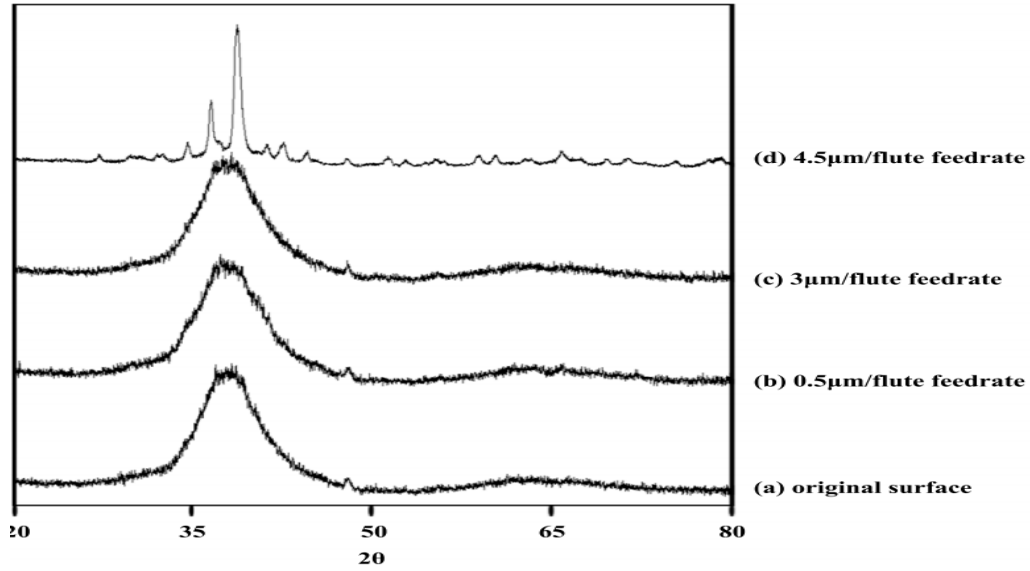
(a)

(b)

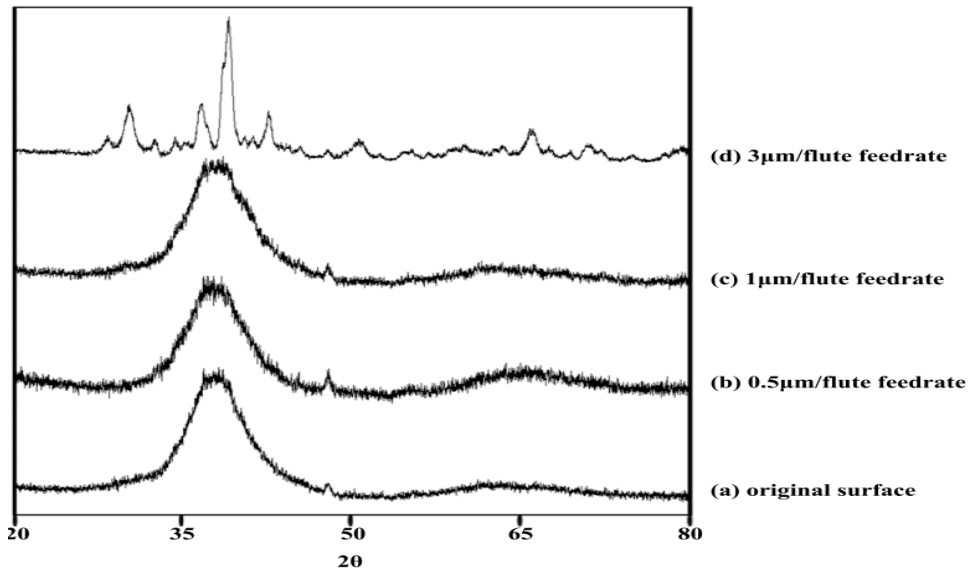
**Figure 3.13** Cross Section of Machined Surface: (a) Test Number 5, Level 2 Light Emission; (b) Test Number 6, Level 3 Light Emission.

### 3.3.3. *Crystallization of workpiece material*

Crystallization of original amorphous microstructure of the workpiece in the milling process was examined through XRD. Figure 3.14 shows the XRD results for the original and the machined surfaces. The machining parameters labeled as (b), (c) and (d) correspond to the process with light emission levels of 1, 2 and 3 respectively. It is observed from the diffraction patterns that the processes with light emission levels of 1 and 2 result in the similar broad peaks covering the same  $\theta$  value as the original surface, representing an amorphous microstructure. However, diffraction pattern corresponding to level 3 of light emission shows strong characteristic peaks, proving that the crystallization of the surface microstructure occurs. Therefore, it is concluded that the crystallization of original amorphous microstructure of workpiece surface is caused by the surface melting and solidification, which are associated with level 3 light emission in the milling process.



(1) Spindle Speed: 50,000 rpm



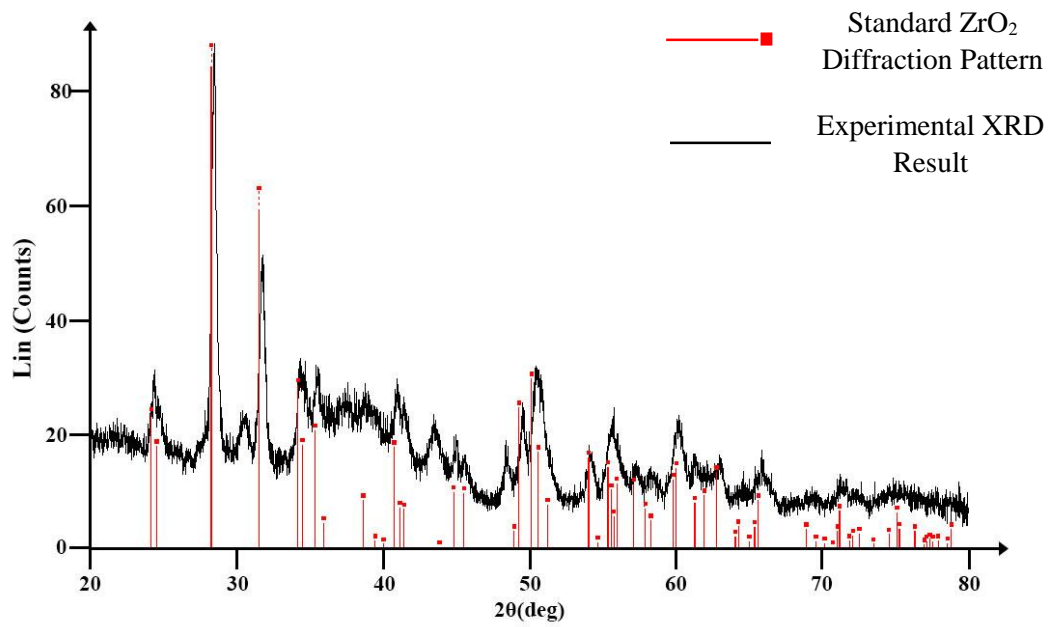
(2) Spindle Speed: 60,000 rpm

**Figure 3.14** Diffraction Patterns of Machined Surface for (a) Original Surface (b) No Spark (c) Little Spark (d) Strong Spark with Melts at 60,000 rpm and 50,000 rpm

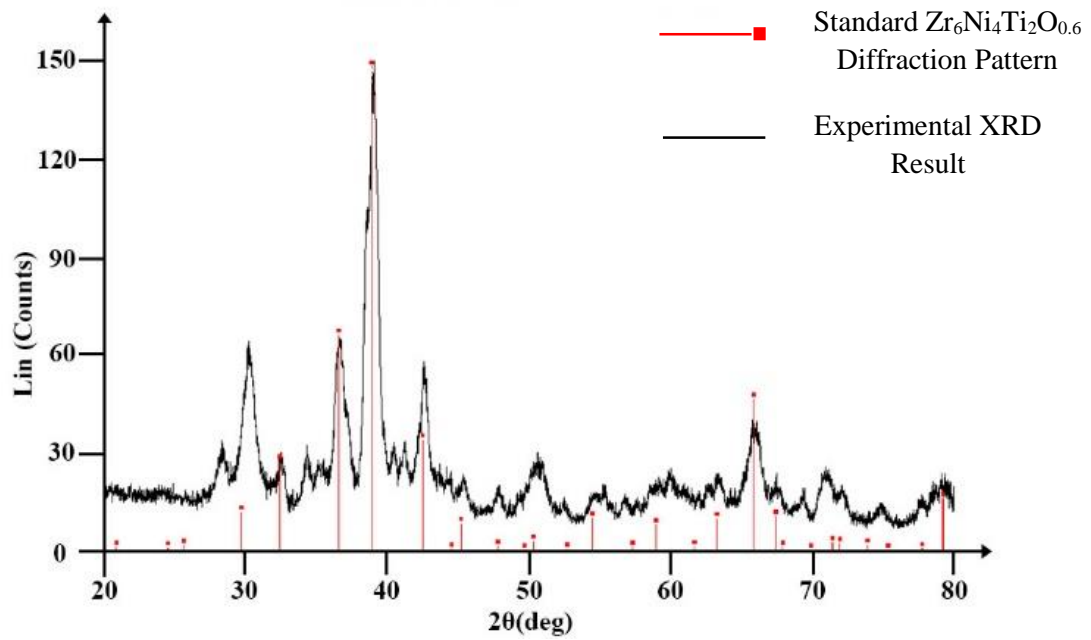
Figure 3.15 shows that crystallization occurs on both chip and machined surface at level 3 light emission, with clear peaks in the XRD results. The experimental XRD curves are compared with standard

---

material diffraction patterns. It is shown that the crystalline phase in the chip is monoclinic  $ZrO_2$ , while the major peaks in the pattern from machined surface correspond to the crystalline phase of  $Zr_6Ni_4Ti_2O_{0.6}$ . The phase difference between the chip and machined surface may be due to the fact that chip carries away most of the heat during machining and is exposed to the oxygen (from air) directly compared to machined surface. These results agree that crystallization is associated with oxidation in machining Zr-BMG. EDS examination was further conducted to confirm the oxidation on crystallized chip and machined surface. Figure 3.16 shows the EDS spectra for the surfaces (original and machined) and chips at level 3 light emission. In Figure 3.16 (a), no oxygen presents in the spectrum of original surface, while the analysis of Figure 3.16 (b) shows that the content of oxygen on the machined surface is more than 10% by weight. Similarly, Figure 3.16 (c) shows the presence of oxygen on the chip. These results demonstrate that the oxidation exists on the machined surface and the chip at the cutting condition corresponding to level 3 light emission.



(a)



(b)

**Figure 3.15** XRD of Chip (a) and Machined Surface (b) (Test Number 6 in Table 3.5)

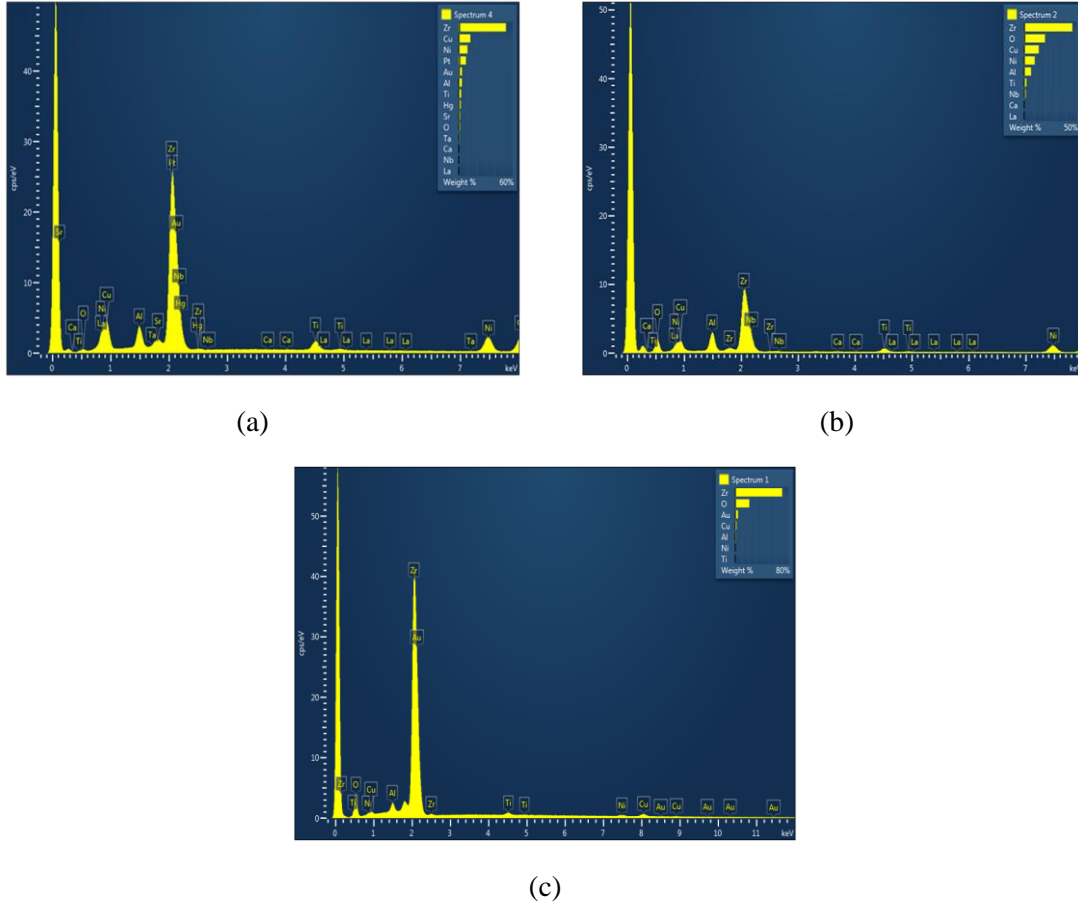


**Figure 3.16** EDS Patterns of (a) Original Surface, (b) Machined Surface at Level 3 Light Emission, (c) Chip at Level 3 Light Emission

Experimental results prove that at constant spindle speed, a higher feedrate intends to cause crystallization of original amorphous workpiece materials due to larger material removal load. A critical feedrate value exists, which corresponds to the onset of surface crystallization. When the feedrate exceeds the critical value, material melting occurs in the milling process, and solidified material forms dark region on the machined surface, leading to surface crystallization of the workpiece. Therefore, there is a need to determine the cutting conditions that can achieve the highest material removal rate without causing crystallization. In this study, a series of experiments were performed to determine the cutting conditions corresponding to the onset of surface crystallization. The spindle speeds varied from 10,000 rpm to 60,000 rpm, with an increment step of 5,000 rpm. At each spindle speed, feedrate gradually increased from 0.5



$\mu\text{m}/\text{flute}$  to  $10 \mu\text{m}/\text{flute}$  with a  $0.5 \mu\text{m}/\text{flute}$  increment, until the surface crystallization was observed. The tool edge geometry after each cut was examined under the microscope to avoid excessive tool wear. The results are listed in Table 3.6. Figure 3.17 shows the identified crystallization transition curve, which represents the cutting conditions corresponding to the onset of surface crystallization. The critical feedrate value decreases asymptotically when the spindle speed increases. Below 30,000 rpm, there was no crystallization even the feedrate increased up to  $10 \mu\text{m}/\text{flute}$ . Based on the identified results, the critical cutting parameters were curve fitted by a power function, expressed as:

$$f = 407200n^{-1.723}$$

where  $f$  is the critical feedrate with the unit of mm/flute, and  $n$  is the spindle speed with the unit of rev/min. The cutting conditions in the region below the transition curve represent the process without surface crystallization, and vice versa.

**Table 3.6** Critical Cutting Conditions for Crystallization Transition

No	Spindle speed (rpm)	Feedrate (mm/flute)
1	60,000	0.0015
2	55,000	0.003
3	50,000	0.0035
4	45,000	0.0040
5	40,000	0.005
6	35,000	0.0065
7	30,000	0.0075
8	25,000	—
9	20,000	—
10	15,000	—
11	10,000	—

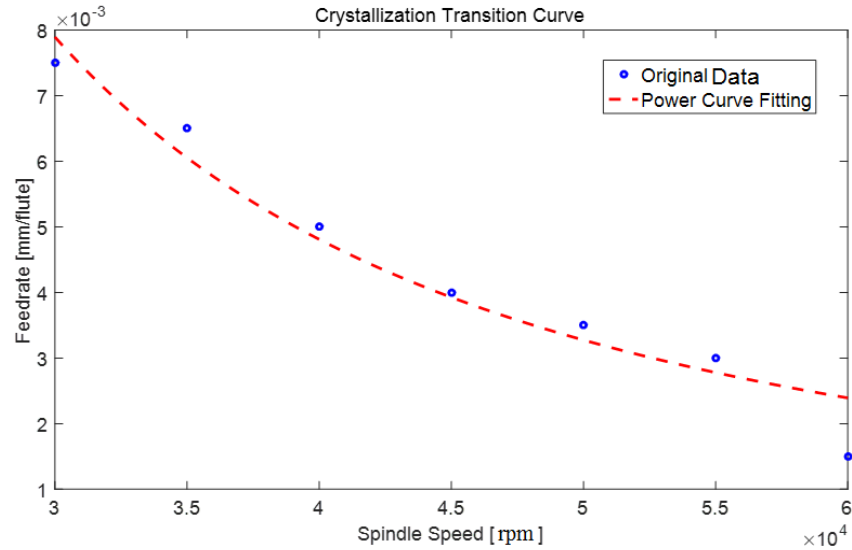


**Figure 3.17** Crystallization Transition Curve

### 3.3.4. Tool wear in micro-milling of Zr-based BMG

Due to the high strength of Zr-based BMG material, fast tool wear and possible edge chipping are frequently observed in the micro-milling process. Tool flank wear changes the material deformation mechanism, and leads to poor surface finish as well as excessive burr formation [59]. Application of coolant has been demonstrated to be effective to reduce tool wear rate in the machining of conventional high-strength metal alloys [60,61]. Using mist coolant is more cost effective and environmentally friendly compared to the flood coolant [62,63]. In this study, the progressive tool flank wear width with respect to the cutting distance was determined at different cutting speeds. The effect of tool wear on light emission, and the effect of mist coolant on tool flank wear were investigated.

#### 3.3.4.1. Tool wear in dry machining condition

In the dry machining process, 0.2 mm radial depth of cut and 1.0  $\mu\text{m}/\text{flute}$  feedrate were used in all the experiments. Higher feedrate was not used since it caused severe tool wear within several machining paths. The spindle speeds ranged from 10,000 rpm to 60,000 rpm in order to determine the effect of machining speeds on the tool flank wear rate. Tool flank face was investigated under SEM, shown in Figure 3.18. It is observed that some extra materials adhere to the flank face of the tool edge after the machining

process, with the formation of build up edge (BUE). EDS analysis was conducted on the adhered material. The output pattern is shown in Figure 3.19. The presence of Zr concludes that the adhered material comes from Zr-BMG workpiece. This result confirms that adhesive wear is the dominant wear mechanism at the tool flank face due to material melting and solidification at the tool edge. For the purpose of tool wear width measurement, milling tool is cleaned by ultrasonic cleaner after the machining experiments. Figure 3.20 shows the comparison of the flank face between a new tool and a tool with flank wear observed under the optical microscope. It is found from Figure 3.20 - (b) that the width of the flank wear is not uniform along the tool edge. Thus, seven measurements of wear width were taken along the edge. The average values are plotted with respect to the milling distance at different spindle speeds, shown in Figure 3.21. Higher spindle speed accelerates the wear rate of tool flank due to higher machining temperature. When spindle speed increases from 10,000 rpm to 60,000 rpm, the tool wear rate is almost doubled. Furthermore, it was found that for the cutting conditions corresponding to level 2 light emission, new cutting tool produced light emission in the milling process, which disappeared later when the tool flank wear gradually increased. This is because the progressive tool wear increases the edge radius, and the ploughing effect is more dominant compared to the chip formation due to shearing. As a result, the material volume in the primary deformation zone decreases.

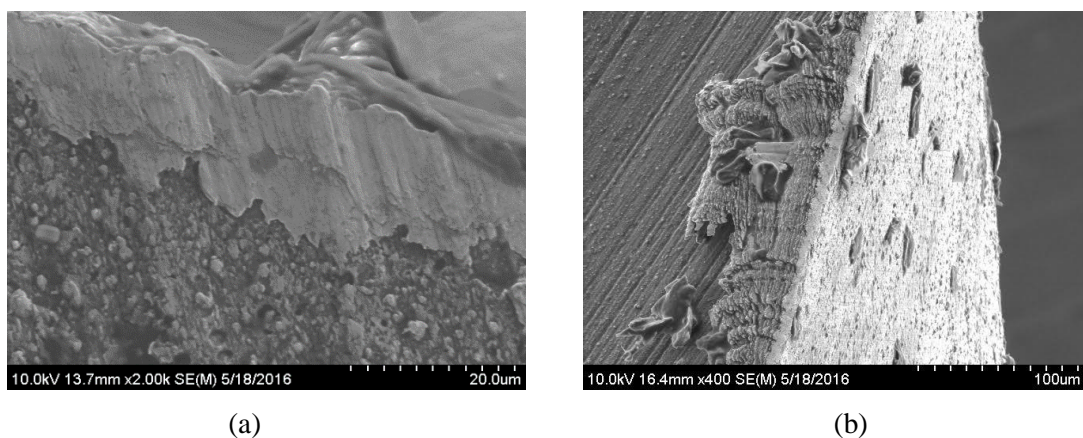


**Figure 3.18** SEM Image of Tool Flank Face after Milling Process (a) BMG Material Adhere to the Flank Face (b) Build Up Edge

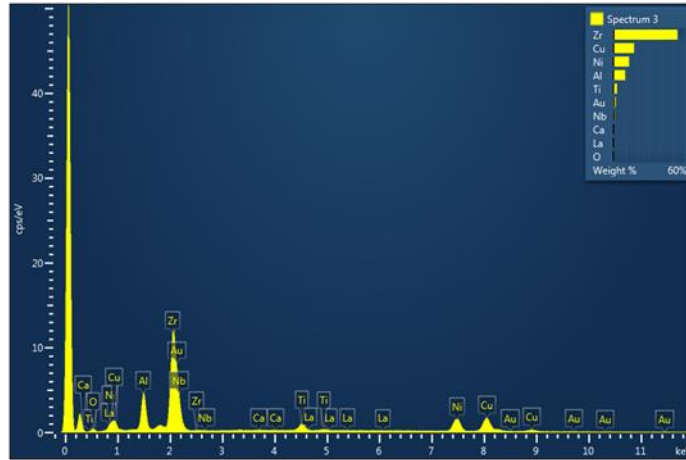


**Figure 3.19** EDS Pattern of the Adhered Material at the Flank Face

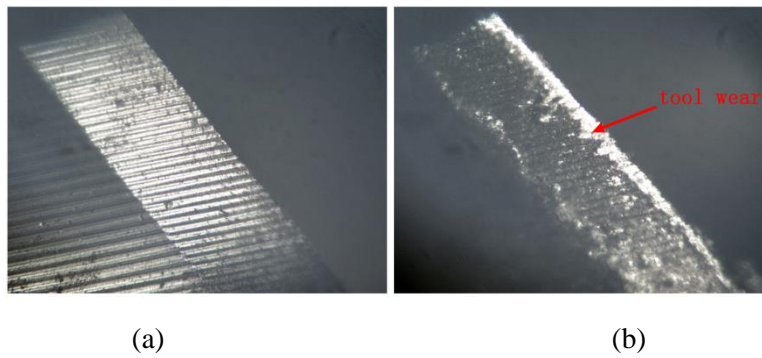


**Figure 3.20** Comparison of New Tool vs Worn Tool (a) New Tool (b) Worn Tool

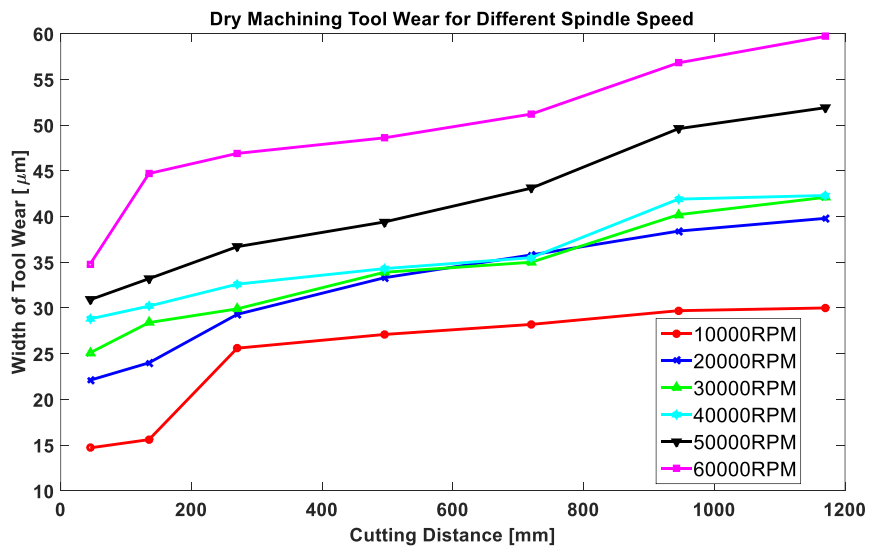


**Figure 3.21** Dry Machining Tool Wear for Different Spindle Speeds

### 3.3.4.2. Tool wear in machining with mist coolant

Mist coolant was used in the micro-milling of Zr-based BMG when the spindle speeds ranged from 40,000 rpm to 105,000 rpm. The progressive tool flank wear corresponding to the cutting distance is shown in Figure 3.22. It was found that tool wear rate increased extensively for the spindle speeds of 90,000 rpm and 105,000 rpm. That is because when spindle speed is less than 90,000 rpm, the light emission is significantly suppressed by the application of mist coolant. However, when the spindle speed increases further, the mist coolant cannot remove enough heat produced by the machining process. The results demonstrate that the light emission in the milling process plays the most significant role in the progressive tool flank wear in the micro-milling of Zr-based BMG. Figure 3.23 shows the comparison of tool flank wear with and without the application of coolant when the spindle speed ranges from 40,000 rpm to 60,000 rpm. It is found that after the light emission was eliminated due to the application of mist coolant, the tool wear rate could be reduced by approximately 75%.

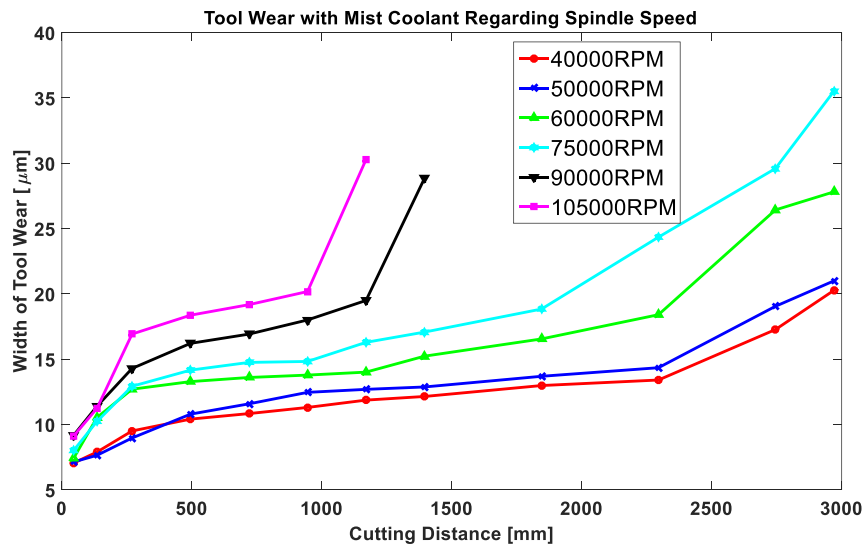
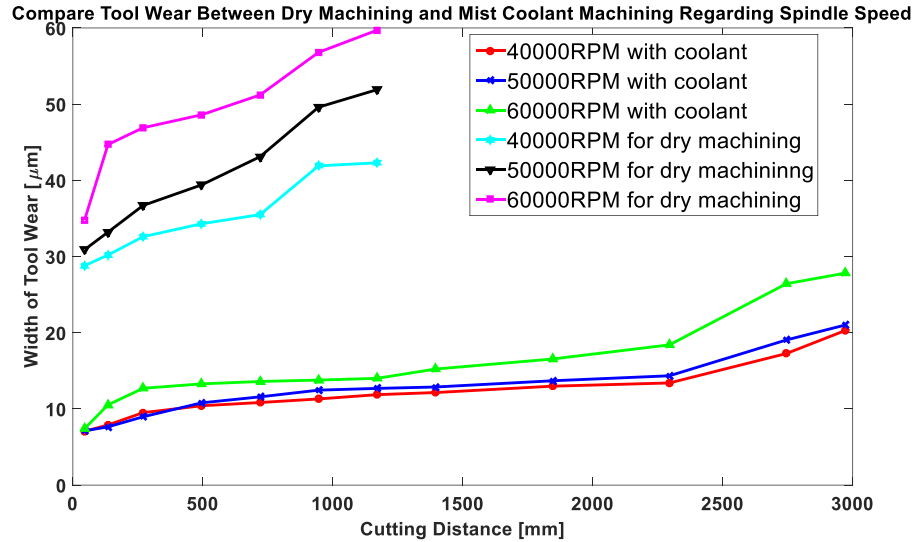


Figure 3.22 Mist-coolant Machining Tool Wear for Different Spindle Speeds



**Figure 3.23** Mist-coolant Machining Tool Wear Vs Dry Machining Tool Wear

### 3.4. Summary

This chapter investigates the machinability of Zr-based BMG material in micro-milling process. The effect of cutting conditions on light emission was investigated and classified into 3 levels. The surface morphology and crystallization were characterized through SEM, metalloscope, XRD and EDS. The constituent elements of machined chip and surface were determined and compared. The critical values of spindle speed and feedrate corresponding to the onset of surface crystallization were identified. Tool flank wear mechanism and the effect on the light emission in the milling of Zr-based BMG was determined, and the effect of mist coolant on the progressive tool flank wear was investigated. The conclusions based on the results are listed below:

- (1) The surface morphology is modified due to the melting and solidification of workpiece material in the milling process. As a result, surface cracks and voids are generated, which are detrimental to the mechanical properties of the machined components.
- (2) Surface melting causes crystallization of the material on both chip and machined surface. However, the remaining constituent elements between the chip and the surface are different. A

---

crystallization transition curve for machined surface exists, which represent the onset of the surface crystallization. The results provide the cutting conditions to achieve maximum efficiency without causing the occurrence of crystallization.

(3) Adhesive wear is the dominant mechanism in tool flank wear in the micro-milling process. Tool wear suppresses the light emission due to ploughing effect with larger tool edge radius. Application of mist coolant is able to reduce tool wear rate by up to 75% by reducing the strength of light emission. However, when spindle speed reach beyond 90,000 rpm, the coolant cannot take away enough heat produced by the machining process, which leads to fast tool wear.

---

## CHAPTER IV

### VIBRATION ASSISTED MILLING OF BK-7 GLASS

#### 4.1. Overview

This chapter presents the study of vibration assisted micro-milling of BK7 optical glass. A CNC milling machine and diamond coated milling tool were used to conduct the experiments. A two-dimensional vibration stage with thin-wall structures to induce vibration was developed. The dynamic property of the vibration stage was analyzed and identified. The effects of vibration direction, amplitude and frequency on the surface roughness and surface damage were investigated.

Vibrations were generated by piezo actuators (model P844.10) from PI, which were driven by amplifiers (model TS-200-1) from Accel Instruments with a wide bandwidth of 0-11 KHz. The output voltage and current could reach up to 20 V and 3 A under 8 kHz frequency. A waveform generator (model BK Precision 4055) was used to generate sinewave signal. A dynamic signal acquisition module (model NI USB 4432) was used to collect data from a displacement sensor, then the data was transmitted to a laptop. The schematic of the experimental system is shown in Figure 4.1



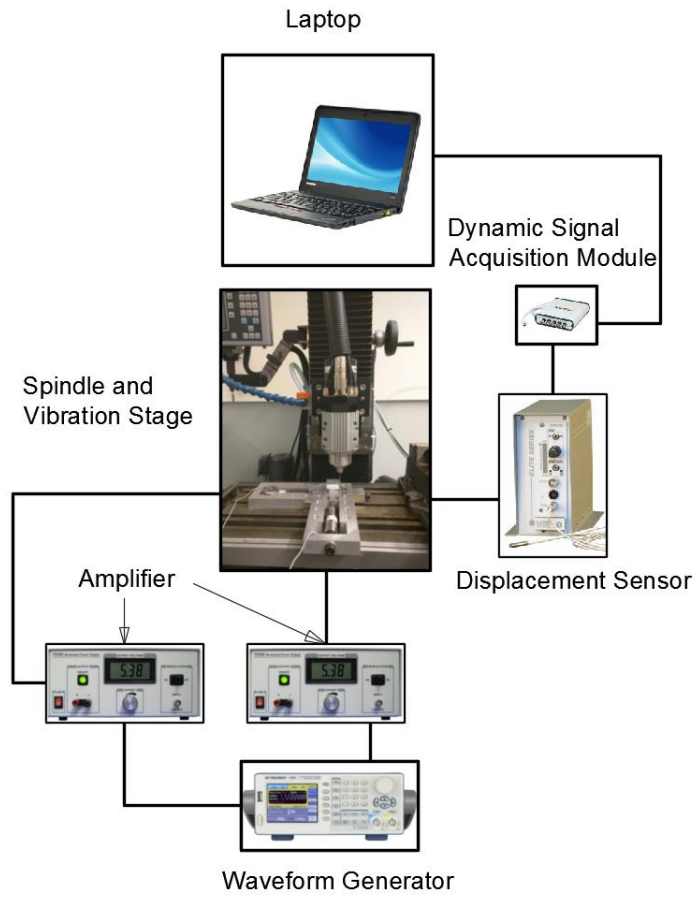


**Figure 4.1** Schematic of Experimental System

#### **4.2. Design of the 2-D Vibration Stage**

A 2-D vibration stage was designed to drive the workpiece in the micro-milling process. The flow chart of designing the vibration system is shown in Figure 4.2.

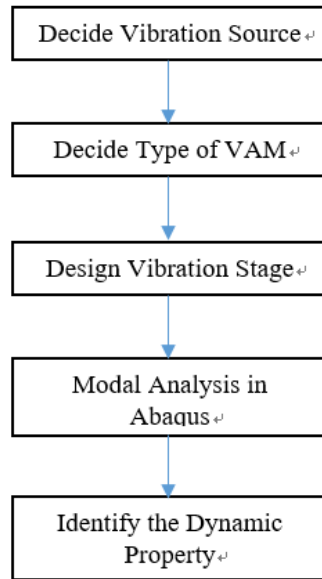


**Figure 4.2** Design Process for Vibration System

#### 4.2.1. *Vibration source*

In the VAM process, vibration assistance is provided either by the spindle or by workpiece to modify the relative motion between the tool and the workpiece. In this study, due to the small mass of the workpiece used in the micro-milling process, vibration was applied to the workpiece by developing a vibration stage. In this way, various values of vibration frequencies and amplitudes could be achieved, depending on the design of the stage.

#### 4.2.2. *Type of vibration system*

Based on the piezo actuator and required vibration parameters, vibration systems can be resonant systems or non-resonant systems. In this thesis, P844.10 piezo actuators from Physik Instrument were used with the specification and required vibration parameters listed in Table 4.1.

**Table 4.1** (a) Specification for P844.10 Piezo Actuator [64] (b) Required Vibration Parameters

Travel distance for 0 to 100V [ $\mu\text{m}$ ] $\pm 20\%$	Static large-signal stiffness [ $\text{N}/\mu\text{m}$ ] $\pm 20\%$	Push/Pull force capacity [N]	Electrical capacitance [ $\mu\text{F}$ ] $\pm 20\%$
15	225	3000/700	6.0
Dynamic Operating current coefficient [ $\mu\text{A}/(\text{Hz}\cdot\mu\text{m})$ ]	Resonant frequency (unloaded) [kHz] $\pm 20\%$	Mass without cable [g] $\pm 5\%$	Length L [mm]
50	16	84	47

(a)

Frequency range kHz	Amplitude range $\mu\text{m}$
5~10	10 $\mu\text{m}$

(b)

The relationship between the displacement  $\Delta L_0$  and the generated force  $F$  of the piezo actuator under different input voltages is expressed in Figure 4.3. An amplifier is used to generate a maximum output voltage of 20 V. According to the piezo actuator specification and amplifier maximum output voltage, the maximum output displacement and forces on the tip of the actuator are

$$\Delta L_{0max} = 15\mu\text{m} \times \frac{20\text{V}}{100\text{V}} = 3\mu\text{m}$$

$$F_{push\ max} = 3000\text{N} \times \frac{20\text{V}}{100\text{V}} = 600\text{N}$$

$$F_{pull\ max} = 700\text{N} \times \frac{20\text{V}}{100\text{V}} = 140\text{N}$$

The curves in Figure 4.3 show that  $\Delta L_0$  varies inversely with  $F$ , therefore, the maximum displacement and Push/Pull force cannot be reached at the same time. Since the piezo actuator cannot achieve more than 3  $\mu\text{m}$  displacement, a vibration stage with thin-wall structures and resonance mechanism is designed and developed.

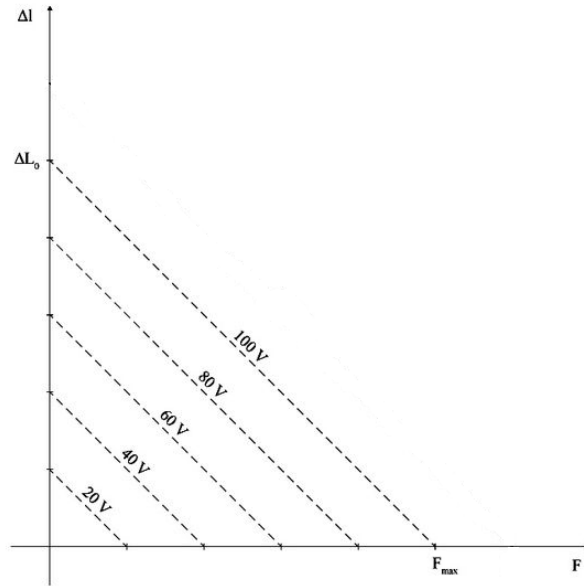
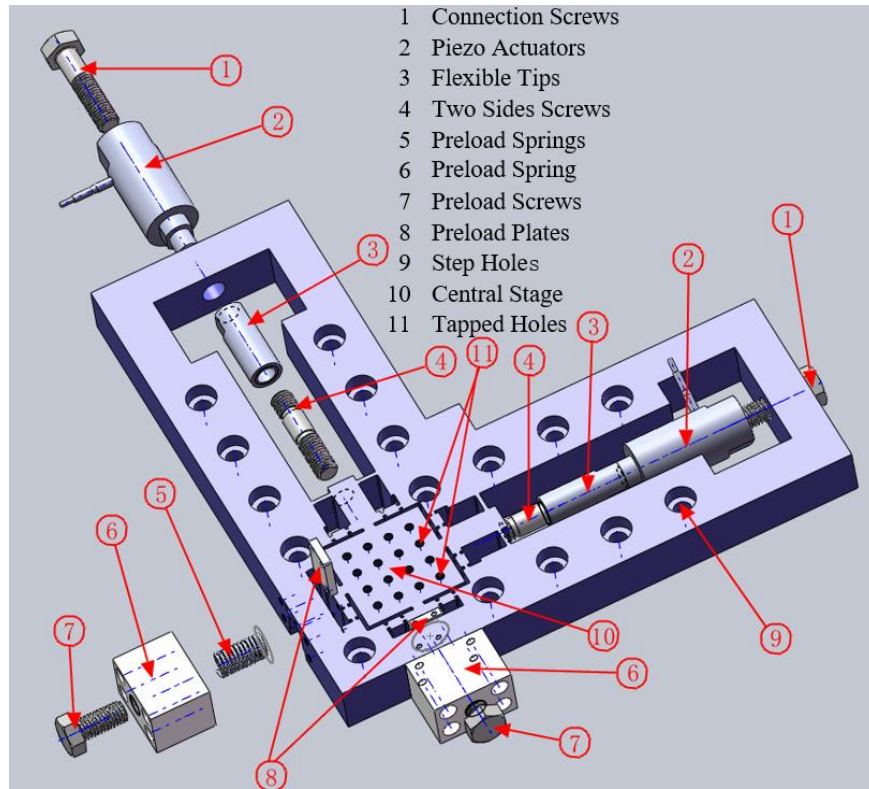


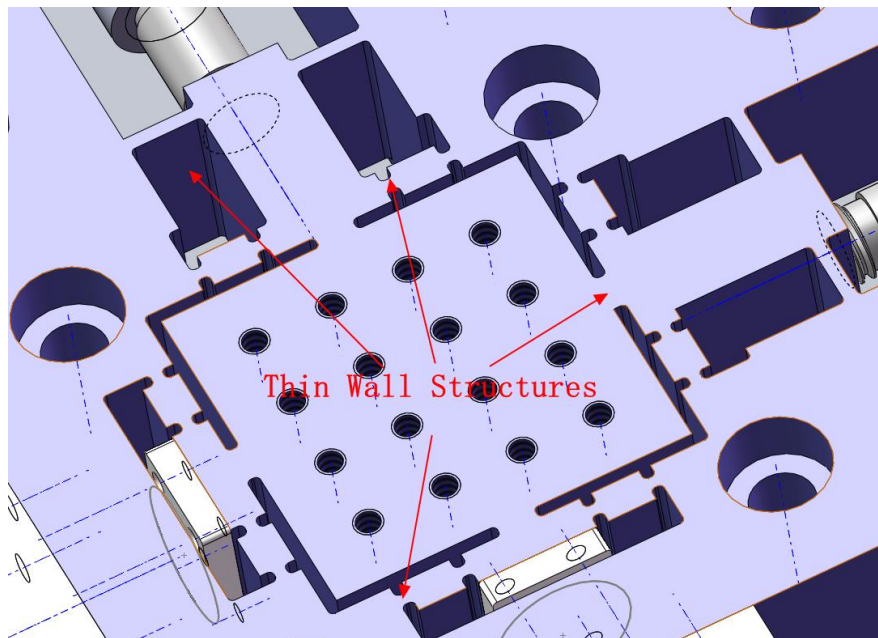
**Figure 4.3** Working Graph of Actuator with Unipolar Operation at Different Voltage Levels

#### 4.2.3. Design of vibration stage

The mechanical structure of the vibration stage is illustrated in Figure 4.4. The thin-wall structures were designed to transmit the vibration from the piezo actuator to the central stage. The natural frequencies of the stage depend on the thickness of the thin-wall structure. The vibration stage was fixed on the CNC work table through the step holes. Shear force is unavoidable in this structure, because two piezo actuators were arranged in a perpendicular orientation. The generated shear force can easily damage the piezo actuator, thus flexible tips were used for protection. When the shear force is applied, the flexible tips will bend instead of the piezo actuators. The piezo actuator is sensitive to the pulling force. Thus, two preload structures were added to the vibration stage to balance the pulling force. By using the preload screw, the springs inside are compressed and a preload can be applied. The tapped holes in the central stage are used to attach the workpiece.



(a)



(b)

**Figure 4.4** Vibration Stage (a) Basic Design (b) Thin-wall Structures

---

#### 4.2.4. *Vibration stage vibration analysis*

The resonant frequency of the stage depends on the design of the structure. Finite element (FE) method was implemented for modal analysis of the vibration stage to predict the natural frequencies. A flow diagram of the analysis process is presented in Figure 4.5. The material of the vibration stage is Al-6061 alloy. The material properties are listed in Table 4.2. The boundary condition was provided by fixing the bottom of the stage as shown in Figure 4.6. In the FE analysis, the vibration stage was meshed by 41052 elements. The natural frequencies of the stage can be adjusted by modifying the thickness of the thin-wall structures. Thicker walls increase the natural frequency and thinner walls decrease the natural frequencies due to the change in stiffness. After the trial and error process, it is found that 2.5mm thickness walls result in the natural frequencies of the stage being 8201 Hz and 8194 Hz. The mode shapes that the center stage vibrates along in X and Y directions are shown in Figure 4.7. Wire Electrical Discharge Machining (WEDM) was used to manufacture the thin-wall structures for the stage. Higher thickness was not considered as it increased the manufacturing difficulty. All of the mode shapes under 20 kHz are listed in Table 4.3.

**Table 4.2** Vibration Stage Material Properties

Mass density [T/mm <sup>3</sup> ]	Young's Modulus [MPa]	Poisson's Ratio
$2.7 \times 10^{-6}$	$69 \times 10^6$	0.33

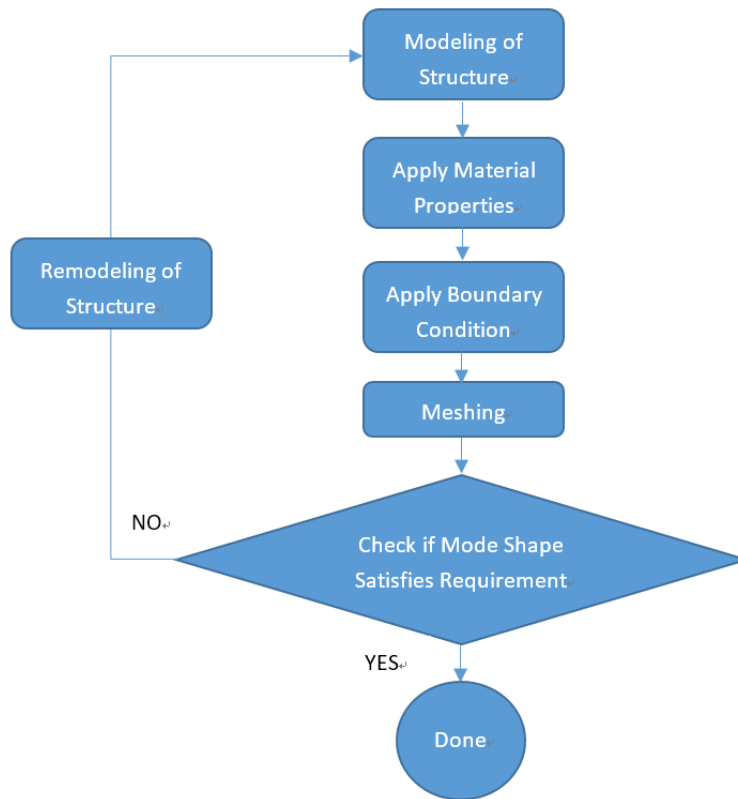


**Figure 4.5** Design Process Flow Chart

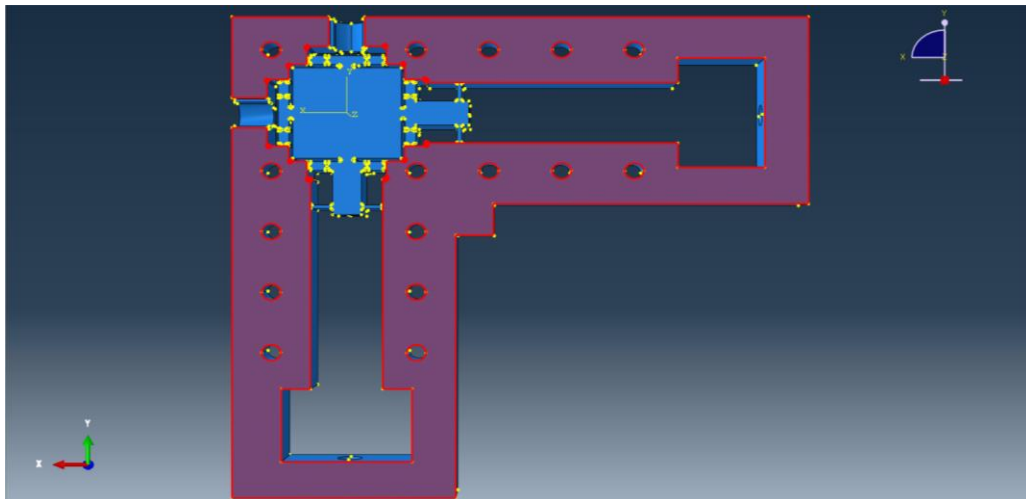
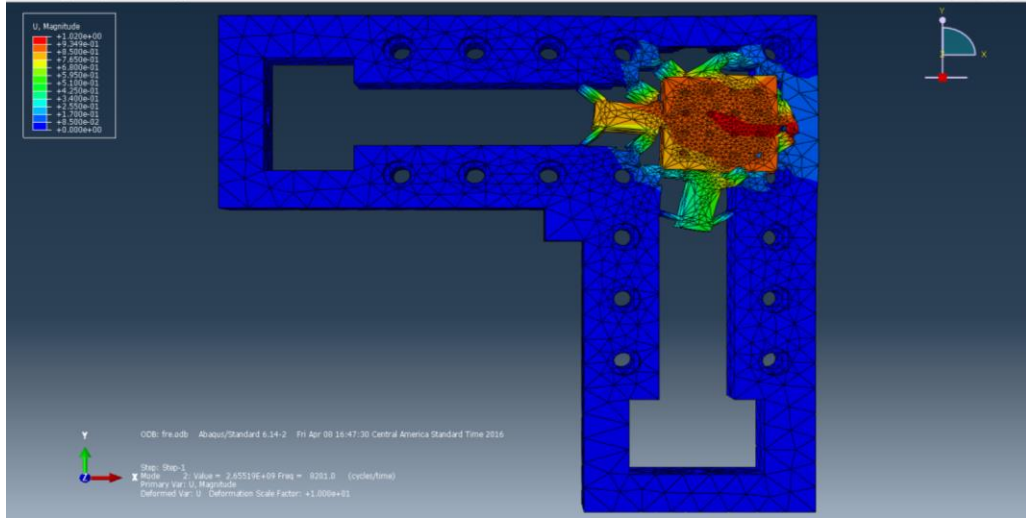
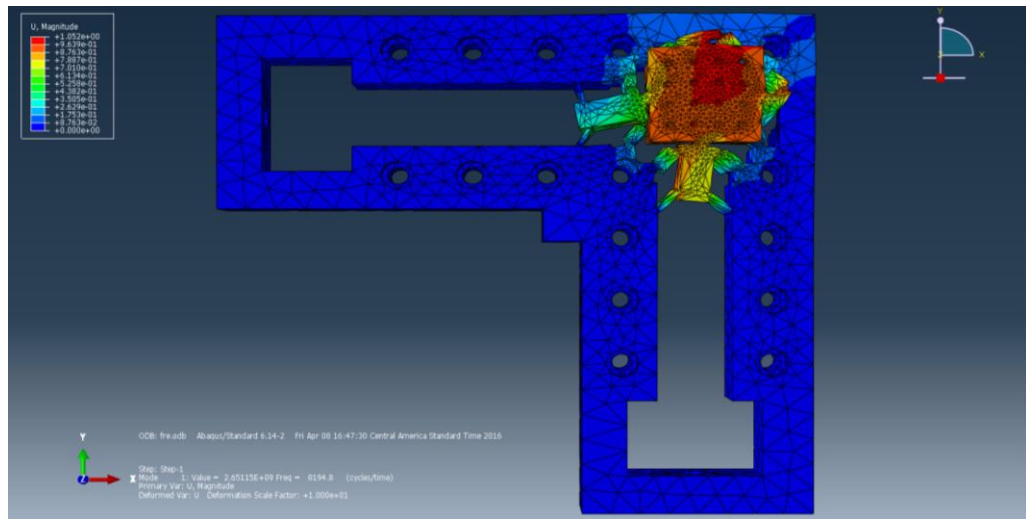


**Figure 4.6** Vibration Stage Boundary Condition



(a)

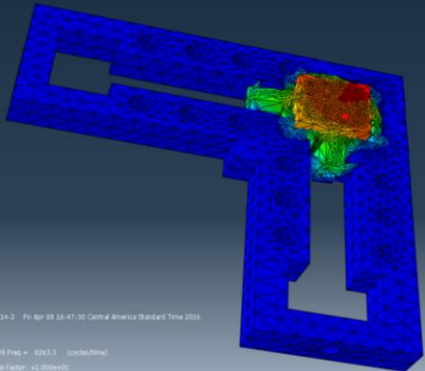
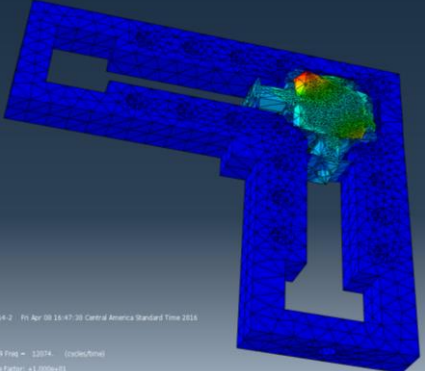
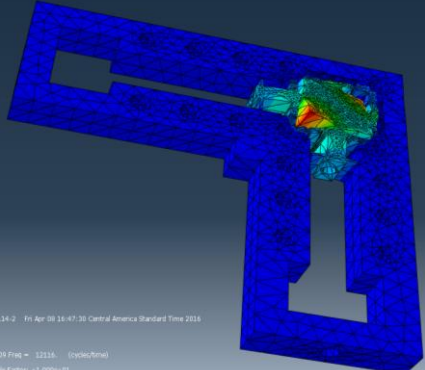
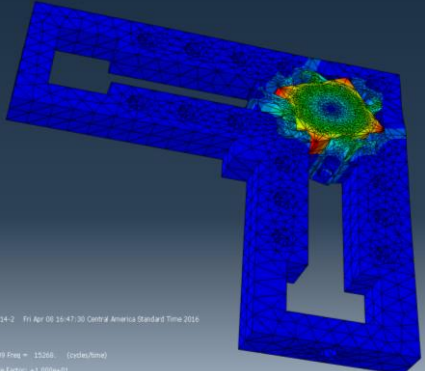


(b)

**Figure 4.7** Desired Mode Shapes at (a) 8201Hz (b) 8194Hz



**Table 4.3** Vibration Stage Mode Shapes under 20 kHz

Frequency [Hz]	Mode shape
8263	 <p>14-2 Fri Apr 09 16:47:30 Central America Standard Time 2016          10 Freq = 8263.3 (cycles/min)          11 Factor = +1.000e+02</p>
12074	 <p>14-2 Fri Apr 09 16:47:30 Central America Standard Time 2016          10 Freq = 12074 (cycles/min)          11 Factor = +1.000e+01</p>
12116	 <p>14-2 Fri Apr 09 16:47:30 Central America Standard Time 2016          10 Freq = 12116 (cycles/min)          11 Factor = +1.000e+01</p>
15268	 <p>14-2 Fri Apr 09 16:47:30 Central America Standard Time 2016          10 Freq = 15268 (cycles/min)          11 Factor = +1.000e+01</p>

#### 4.2.5. Identification of the dynamic property

After the vibration stage was fabricated, a series of vibration tests were conducted to experimentally identify the dynamic property of the vibration stage. The frequencies of the input voltage to the amplifier were swept up to 11 kHz, and a Lion Precision displacement sensor (model CPL-290) was used to measure the displacement of the vibration stage.

The specification of the displacement sensor is given in Table 4.4. This displacement sensor was connected with a 5 mm diameter probe. The probe was supported by a probe-holder, which was glued on to the stationary part of vibration stage (Figure 4.8).

**Table 4.4** CPL-290 Specification [65]

Linearity Error	±0.2% F. S. or better, dependent on calibration		
Error Band	±0.3% F. S. or better, dependent on calibration		
Probe Interchangeability	Typical sensitivity variation for same probe model: 10%		
Typical Oscillator Frequency	Probe cable < 12 feet: 1 MHz		
	Probe cable > 12 feet: 500 kHz		
Thermal Stability	0.02% F.S./°F, 0.04% F.S./°C		
Coarse Zero Adjustment	±10 VDC	Fine Zero Adjustment Range	±1 VDC
Meets ANSI/ASME B5.54 Standard	Yes	Standard Bandwidth (-3 db)	15 kHz -10%+30%
Operating Temperature	4°-50°C	Output Impedance	0 Ω
Output Max Voltage	±13.5	Output Max Current	10 mA

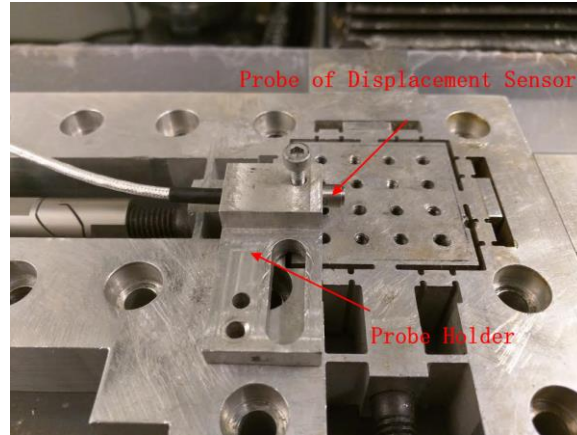


**Figure 4.8** Displacement Sensor Probe Holder

The data collected by the displacement sensor was transmitted to the computer through a dynamic signal acquisition module and then analyzed by CutPro software. As shown in Figure 4.9, the amplitude of vibration varied with time and had an average value of zero. The peak-to-peak value of the displacement signal was recorded.

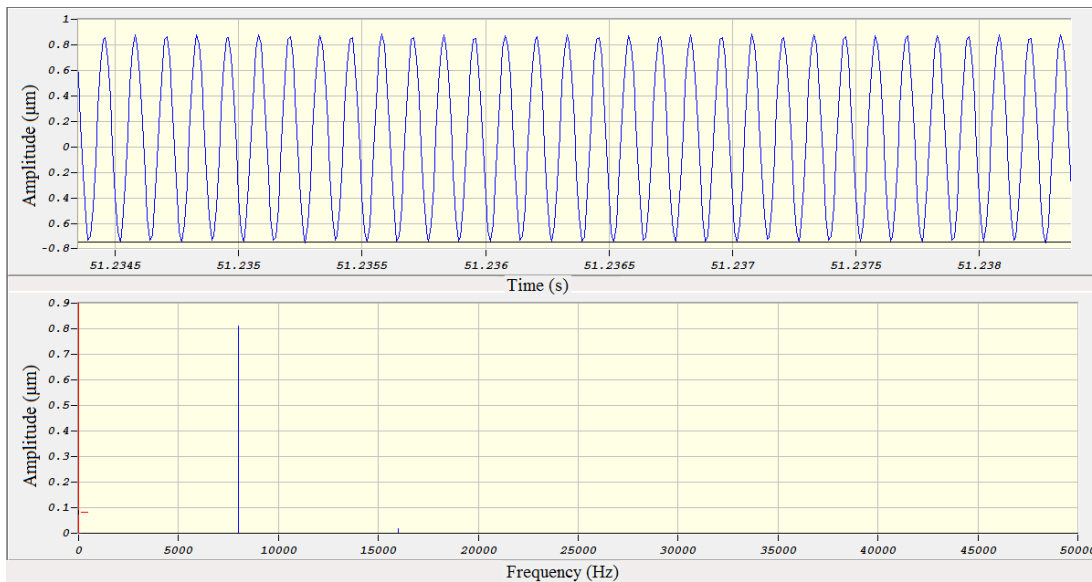


**Figure 4.9** Displacement Measured by CutPro

When the frequency of the input voltage went beyond 11 kHz, the output signal of the amplifier was distorted. The experimentally obtained frequency response functions (FRF) of the vibration stage in X

and Y directions are shown in Figure 4.10. It was found that the stage displacement was amplified in the frequency range of 5-11 kHz. Under each frequency, the relationship between the displacement and the input voltage was calibrated. In the micro-milling experiment, the maximum input voltage was constrained to ensure a linear displacement-voltage relationship.

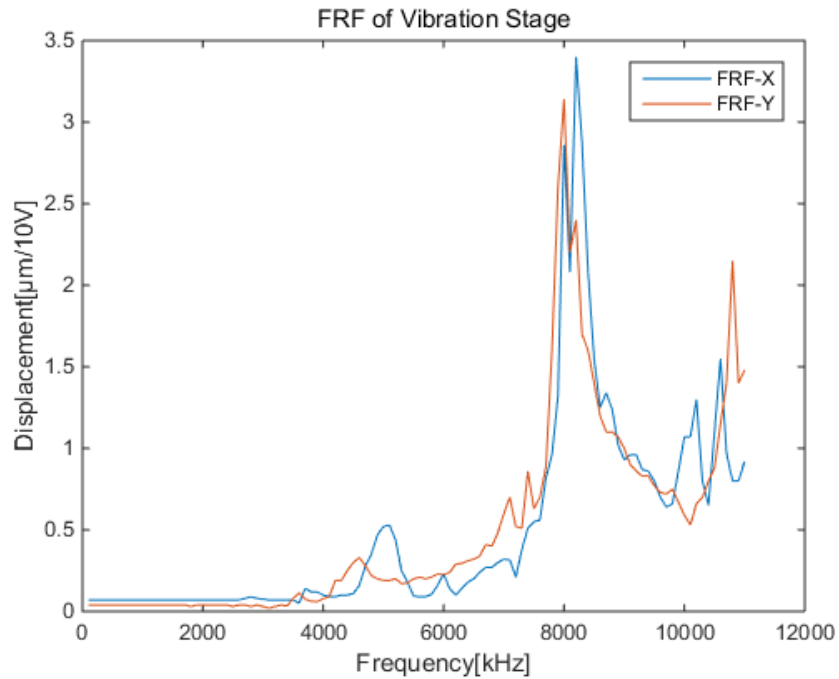


**Figure 4.10** Frequency Response Function of the Vibration Stage

### 4.3. Experimental setup

The vibration assisted micro-milling experiment was conducted on a MDA precision micro-machining center (Figure 3.1 (a)) with a maximum spindle speed of 60,000 rpm. A two-flute diamond coated micro end mill (MICROCUT) with 3.175 mm diameter and 30° helix angle was used. The workpiece was BK-7 uncoated optical glass. The properties of the glass material are listed in Table 4.5. The workpiece was glued onto a small aluminate plate, which was clamped to the center of the vibration stage.

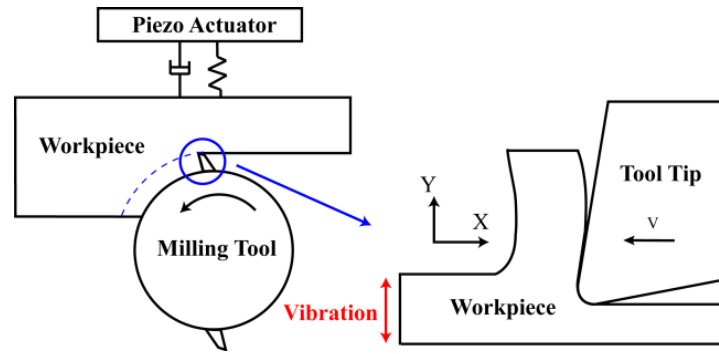
---

**Table 4.5** BK7 Specification [66]

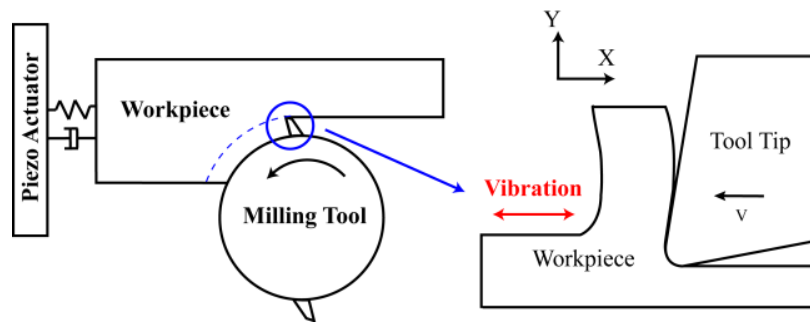
Dimension Tolerance [mm]	±0.25
Dimension [mm]	50 x 50
Thickness [mm]	4.0
Thickness Tolerance [mm]	±0.20
Parallelism [arc min]	5
Surface Accuracy	1λ
Coating	Uncoated
Substrate	N-BK7
Wavelength Range [μm]	0.35-2.2
RoHS	C

#### **4.4. Machining Mechanism of Vibration Assisted Milling Process**

Figure 4.11 shows schematics of micro-milling with vibration assistance in the normal (Y) and feed (X) directions respectively, as well as the chip formation mechanism in the orthogonal representation. When the vibration is applied in the normal direction, the tool edge has a vertical displacement relative to the workpiece, therefore, surface generation is influenced by the tool's indentation beside the shearing mechanism. When vibration is applied in the feed direction, the relative motion between the tool and workpiece is only in the cutting direction, and the surface generation is dominated by the burnishing effect when the tool's bottom edge rubs against the surface.



(a) Vibration in the Normal (Y) Direction.



(b) Vibration in the Feed (X) Direction.

**Figure 4.11** Schematics of Micro-milling with Vibration Assistance in the (a) Normal and (b) Feed Directions.

Figure 4.12 shows the tool tip trajectory with respect to the workpiece when the vibration assistance is provided in the normal direction. The solid curve is a combination of original tool tip motion (dashed line) and high frequency vibration motion in the normal direction. In the vibration assisted micro-milling process, if the tool edge radius is comparable with the amplitude of vibration, the surface is generated when the tool edge indents into the workpiece. The shaded area in Figure 4.12 shows the indentation volume. The indentation increases the hydrostatic pressure in the material deformation zone. As reported by M. Yoshino et al. [67], the hydrostatic pressure enhances the brittle-ductile transition of brittle material. Therefore, this experimental study is to test the hypothesis that the improvement of surface quality is a result of brittle-

---

ductile transition due to the indentation of the tool edge into the workpiece when the vibration assistance is applied.

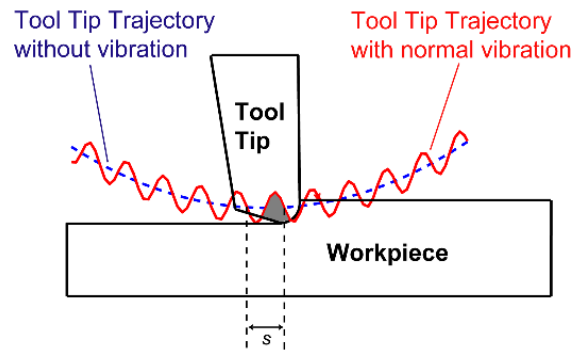


**Figure 4.12** Tool Tip Trajectory with respect to Workpiece with Vibration Assistance in Normal Direction.

#### 4.5. Experimental Process

The cutting conditions of the experiment are listed in Table 4.6. A range of amplitudes and frequencies of vibration assistance were applied to investigate the effect of external vibration on the surface quality. When the uncut chip thickness exceeded the critical value corresponding to the brittle-ductile transition of the glass material, micro cracks were generated on the machined surface. The uncut chip thickness in the milling process was determined by the radial depth of cut and the feedrate. In this study, different values of feedrate and radial depth of cut were applied. The spindle speed and axial depth of cut were kept constant. For each cutting parameter, micro-milling tests were conducted under three vibration assistance conditions: no applied vibration, vibration in the normal direction, and vibration in the feed direction. The cutting tool edges were examined under the optical microscope after each test to avoid severe tool wear. All the tests were repeated three times to ensure repeatability of the results.

**Table 4.6** Cutting Conditions

Vibration	Frequency (kHz)	5, 7, 8, 9, 11
Assistance	Amplitude ( $\mu\text{m}$ )	1.0, 1.2, 2.0, 4.0
Feedrate ( $\mu\text{m}/\text{tooth}$ )		0.4, 0.5
Radial Depth of Cut ( $\mu\text{m}$ )		15, 25
Spindle Speed (rpm)		10,000 rpm
Axial Depth of Cut (mm)		1.0

#### 4.6. Experiment Result

##### 4.6.1. Measurement of surface quality

An SJ-210 Surface roughness tester was used to measure the roughness along the feed direction. The machined surface was cleaned to ensure the accuracy. Measurements for each experiment were performed at 7 different locations to get the average roughness. As the axial depth of cut was only 1.0 mm, in order to make sure the measurements were taken from machining area, the roughness tester was fixed on the spindle, and the workpieces were clamped by vice and with the movement controlled by the CNC (Figure 4.13).

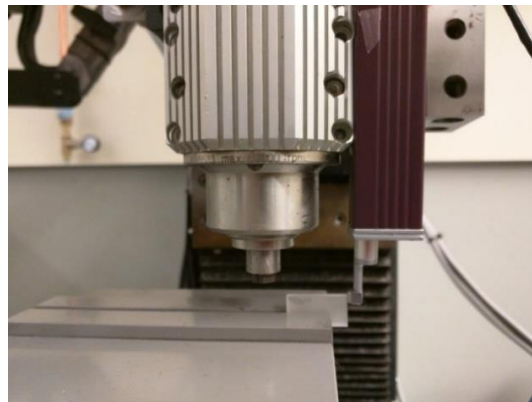


**Figure 4.13** Measure Surface Roughness



---

In addition to the SJ-210, a Nanovea PS50 optical 3-D profilometer with 3.5 mm optical pen was also employed to observe the fractures on the machined surface. The workpieces were placed on the 50 x 50mm stage. The machined surface was scanned at a speed of 2 $\mu$ m/s. Using NANOVEA 3D software, the surface's profile and roughness were obtained.

#### 4.6.2. *Result and analysis*

##### (1) Effect of Vibration Direction and Amplitude on Surface Roughness

Figure 4.14 shows the surface roughness with the vibration amplitudes of 1, 2 and 4  $\mu$ m. A small feedrate of 0.5  $\mu$ m/tooth was selected to ensure a ductile cutting mode. For each vibration amplitude, the surface roughness without external vibration, with vibration applied in the normal and feed directions were compared. The three squares shown in the figure represent repeated tests under no-vibration condition. When the vibration amplitude is 1  $\mu$ m, the variation of surface roughness under the three vibration conditions is less than 2%, showing that vibration assistance with small amplitude is not effective. When the vibration amplitude increases to 2 and 4  $\mu$ m, better surface quality is achieved with vibration assistance. When vibration assistance is applied in the normal direction, the surface roughness decreases by 45% when the vibration amplitude increases from 1  $\mu$ m to 4  $\mu$ m. However, the surface roughness does not change extensively when the vibration applied in the feed direction. Therefore, it is concluded that vibration assistance in the normal direction is the main factor enhancing surface quality improvement. Furthermore, it is found that the surface roughness values decrease asymptotically with the increase in vibration amplitude in the normal vibration mode.

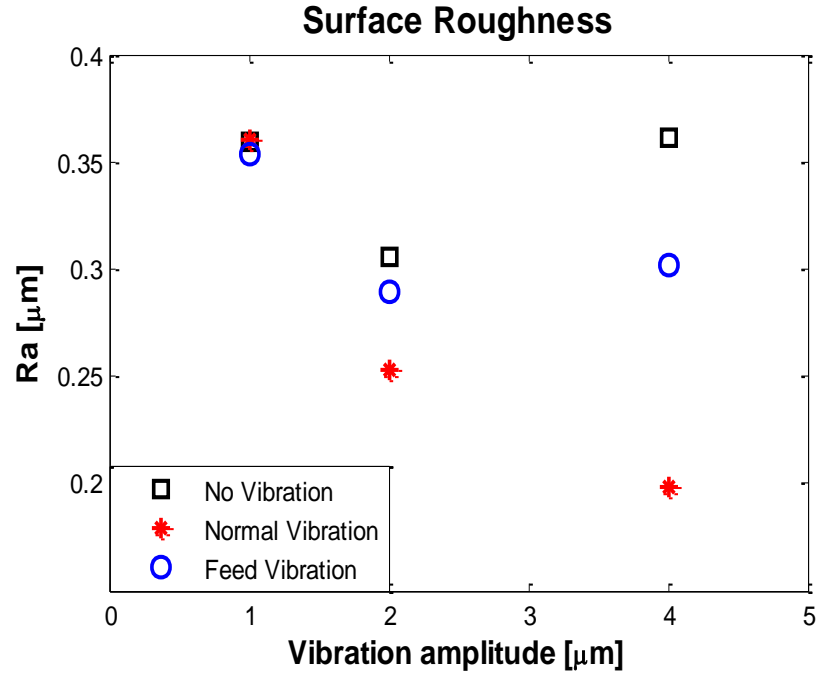


**Figure 4.14** Surface Roughness with Vibration Amplitude. (Frequency: 8 kHz, Feedrate: 0.5  $\mu\text{m}/\text{tooth}$ , Radial depth of cut: 15  $\mu\text{m}$ )

(2) Effect of Vibration Frequency on Surface Roughness

Figure 4.15 shows the surface roughness with respect to the frequency of the vibration with constant vibration amplitude. A frequency range of 5 to 11 kHz was applied. Based on the calibrated FRF of the vibration stage, the vibration displacement at 5 kHz is minimum at 1.2  $\mu\text{m}$  in the linear vibration range. Therefore, constant vibration amplitude of 1.2  $\mu\text{m}$  is applied at all frequencies by adjusting the amplifier's output voltage. It is found that the surface roughness reduces asymptotically when the frequency of applied vibration increases.

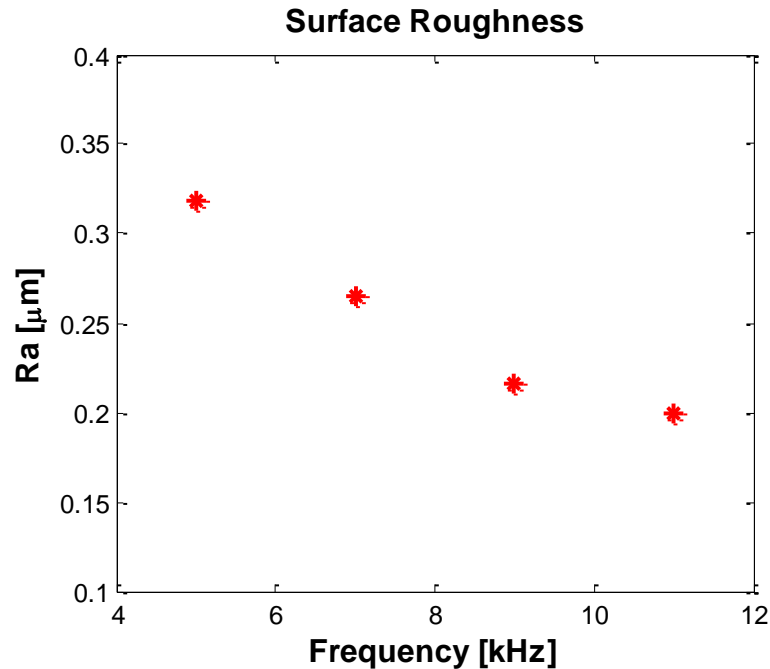


**Figure 4.15** Surface Roughness with Vibration Frequency (Amplitude: 1.2  $\mu\text{m}$ , Feedrate: 0.4  $\mu\text{m}/\text{tooth}$ , Radial depth of cut: 25  $\mu\text{m}$ )

### (3) Effect of Vibration on Surface Damage

In order to determine the effect of vibration assistance on the brittle-ductile transition of glass material, an optical surface profilometer was used to investigate the surface damage after the milling process. A micro-milling tool with a small diameter (0.889 mm) was used to have brittle dominated milling process due to low structural stiffness. Different values of radial depth of cut, feedrate, vibration frequency and amplitude were used. Table 4.7 shows the conditions of two cutting tests, with the side surface profile presented in Figure 4-16 (a) and (b). Each surface figure corresponds to a single tool pass, with the left hand side representing vibration assisted milling in the normal direction, and the right hand side portion representing milling without vibration. The dark regions in the pictures show the voids left on the machined surface, which indicates occurrence of brittle deformation in the milling process. It is found that when the vibration is applied, surface damage decreases extensively. Therefore, it is concluded that vibration

assistance in the normal direction enhances the brittle-ductile transition of the material in the micro-milling of glass.

**Table 4.7** Surface Profile Measured by Optical Profilometer

Axial Depth of Cut (mm)		0.5	
Spindle Speed (rpm)		10000	
FeedRate ( $\mu\text{m}/\text{tooth}$ )		1.0	
		Test (a)	Test (b)
Vibration Assistance	Frequency (kHz)	4	11
	Amplitude ( $\mu\text{m}$ )	0.8	0.5
Radial Depth of Cut ( $\mu\text{m}$ )		15	3

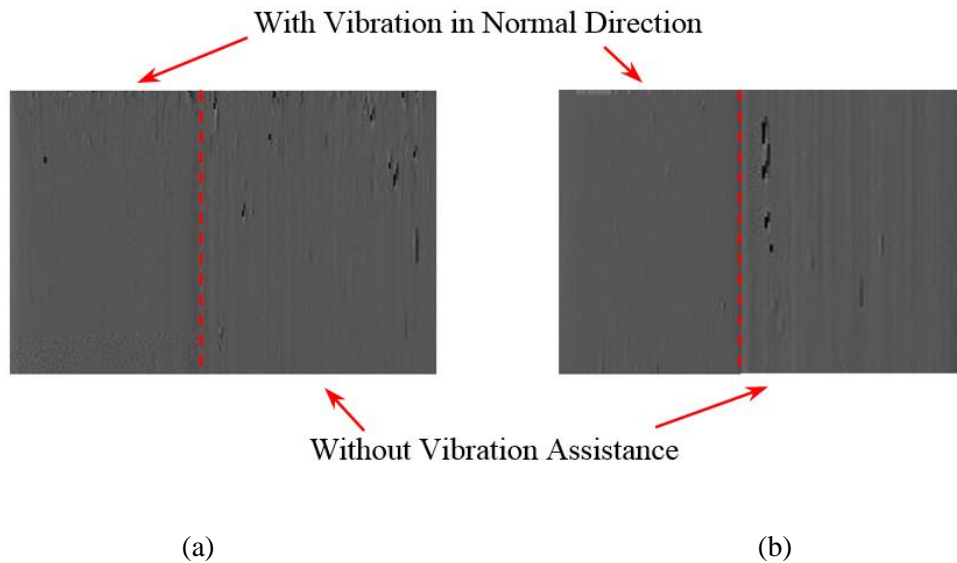


**Figure 4.16** Comparison of Surface Profile with and without Vibration Assistance

#### 4.7. Summary

This chapter investigates the machinability in 2-D vibration assisted micro-milling of optical glass. The experiments were conducted on BK-7 optical glass with 3.175 mm and 0.889 mm diameter milling tools. A two dimensional vibration stage was developed based on a thin-wall design with piezoelectric

---

actuators. The natural frequencies and mode shapes of the vibration stage were analyzed using a finite element method and the frequency response function of the vibration was experimentally calibrated. The effect of vibration direction, amplitude and frequency on the micro-milling performance was studied. The surface damage was characterized by the profilometer. The surface roughness was measured through a roughness tester. Base on the results, it is concluded that the vibration assistance in the normal direction is the main factor for the improvement of the surface quality. Furthermore, higher vibration frequency and amplitude result in lower surface roughness.

---

## CHAPTER V

### CONCLUSIONS AND RECOMMENDATIONS

#### 5.1. Conclusion

This thesis presents an experimental study of the machinability in the micro-milling of typical amorphous materials, including Zr-BMG and BK-7 glass. A three-axis micro-milling machine was developed to achieve high spindle speed up to 160,000 rpm. In the machining of Zr-BMG, the effect of cutting condition on light emission was investigated, and the microstructure of the machined surface was characterized by XRD, SEM and metalloscope. The cutting conditions corresponding to the onset of material crystallization was determined and verified. The effect of mist-coolant on progressive tool flank wear was determined. The following conclusions are drawn:

(1) Light emission in the micro-milling of Zr-BMG can be classified into 3 levels: no light emission, light without material melting, and light associated with melting. The first two levels do not cause crystallization on the machined surface material based on the XRD analysis. However, surface melting in the third level is associated with the crystallization, resulting in a cracked surface with voids.

(2) The cutting conditions corresponding to the onset of surface crystallization is experimentally determined, and the results provide the spindle speed and feedrate values that do not cause modification of surface microstructure.

---

(3) High cutting temperature in the micro-milling of Zr-BMG causes fast tool flank wear. Applying mist-coolant reduces the tool wear rate by up to 75%, since it eliminates the heat in the machining process and decreases the friction. However, the efficiency of the coolant highly depends on the strength of the light emission.

Vibration assisted micro-milling of BK-7 optical glass was performed. It is concluded that the vibration assistance in the normal direction causes the tool's indentation into the workpiece, while vibration in the feed direction causes the burnishing effect on the surface. The indentation increases the hydrostatic pressure in the tertiary deformation zone, therefore enhancing the brittle-ductile transition of the workpiece material and improving the surface quality. A two dimensional vibration stage was developed based on thin-wall design with piezoelectric actuators. The frequency response function of the vibration was experimentally calibrated. The following conclusions were drawn based on the results:

(1) Surface roughness decreases when vibration-assistance is applied in the micro-milling process. Vibration applied in the normal direction has a major effect on the surface quality improvement due to the application of hydrostatic pressure.

(2) When vibration is applied in the normal direction, higher vibration amplitude results in higher hydrostatic pressure in the tertiary deformation zone, therefore reducing the surface roughness. Higher frequency in the applied vibration reduces the waviness of the surface and improves the surface quality.

(3) The characterization of surface damage proves the enhancement of brittle-ductile transition when normal vibration is applied in the micro-milling of glass material.

## **5.2. Recommendations for Future Work**

In the VAM process, the periodic separation between the tool and the workpiece causes high-frequency variations in the temperature and stress in the material deformation zone. The effect of VAM on chip formation and surface generation in the machining of BMG materials is suggested for future

---

investigation. Furthermore, the real-time measurement of temperature is a challenge due to the small size of the cutting area and high-frequency tool-workpiece contact in the micro-milling of BMG. The commonly used infrared camera has limitations in both spatial and temporal resolutions. New techniques for determining the cutting temperature need to be investigated to study the material removal mechanism in the micro-milling of BMG.



---

## References

- [1] Telescope. Retrieved from <http://www.visioncareinc.net/technology>.
- [2] Micro camera. Retrieved from <https://www.elektormagazine.com/news/heptagon-announce-3d-array-camera>.
- [3] Lejeune, M., Chartier, T., Dossou-Yovo, C., & Noguera, R. (2009). Ink-jet printing of ceramic micro-pillar arrays. *Journal of the European Ceramic Society*, 29(5), 905–911.
- [4] Suryanarayana, C., & Inoue, A. (2011). *Bulk metallic glasses*. Boca Raton, FL: CRC Press.
- [5] Golf clubs made of bulk metallic glass. Retrieved from [http://web.ornl.gov/info/ornlreview/v38\\_1\\_05/article17.shtml](http://web.ornl.gov/info/ornlreview/v38_1_05/article17.shtml).
- [6] Phone case made of bulk metallic glass. Retrieved from <http://supercoolmetals.com/>.
- [7] Chae, J., Park, S. S., & Freiheit, T. (2006). Investigation of micro-cutting operations. *International Journal of Machine Tools and Manufacture*, 46(3), 313-332.
- [8] Rahman, M., Lim, H. S., Neo, K. S., Kumar, A. S., Wong, Y. S., & Li, X. P. (2007). Tool-based nanofinishing and micromachining. *Journal of Materials Processing Technology*, 185(1), 2-16.
- [9] Altintas, Y., & Jin, X. (2011). Mechanics of micro-milling with round edge tools. *CIRP Annals-Manufacturing Technology*, 60(1), 77-80.
- [10] Jin, X., & Altintas, Y. (2013). Chatter stability model of micro-milling with process damping. *Journal of manufacturing science and engineering*, 135(3), 031011.
- [11] Bakkal, M., Shih, A. J., & Scattergood, R. O. (2004). Chip formation, cutting forces, and tool wear in turning of Zr-based bulk metallic glass. *International Journal of Machine Tools and Manufacture*, 44(9), 915-925.
- [12] Bakkal, M., Liu, C. T., Watkins, T. R., Scattergood, R. O., & Shih, A. J. (2004). Oxidation and crystallization of Zr-based bulk metallic glass due to machining. *Intermetallics*, 12(2), 195-204.
- [13] Arif, M., Rahman, M., & San, W. Y. (2011). Ultraprecision ductile mode machining of glass by micromilling process. *Journal of Manufacturing Process*, 13(1), 50–59.
- [14] Moriwaki, T., & Shamoto, E. (1995). Ultrasonic elliptical vibration cutting. *CIRP Annals-Manufacturing Technology*, 44 (1), 31-34.
- [15] Liu, D., Cong, W., Pei, Z. J., & Tang, Y. (2012). A cutting force model for rotary ultrasonic machining of brittle materials. *International Journal of Machine Tools and Manufacture*, 52 (1), 77-84.
- [16] Brehl, D., Dow, T., Garrard, K., & A. Sohn (1999) Micro-Structure Fabrication Using Elliptical Vibration-Assisted Machining (EVAM). *ASPE Proceedings*, 39, 511-515.
- [17] Moriwaki, T., Shamoto, E., & Inoue, K. (1992). Ultraprecision ductile cutting of glass by applying ultrasonic vibration. *CIRP Annals-Manufacturing Technology*, 41 (1), 141-144.
- [18] Xu, W. X., & Zhang, L. C. (2015). Ultrasonic vibration-assisted machining: principle, design and application. *Advances in Manufacturing*, 3(3), 173–192.
- [19] Weber, H., Herberger, J., & Pilz, R. (1984). Turning of Machinable Glass Ceramics with an Ultrasonically Vibrated Tool. *CIRP Annals - Manufacturing Technology*, 33(1), 85–87.
- [20] Shamoto, E., & Moriwaki, T. (1994). Study on Elliptical Vibration Cutting. *CIRP Annals - Manufacturing Technology*, 43(1), 35–38.
- [21] Nath, C., Rahman, M., & Andrew, S. S. K. (2007). A study on ultrasonic vibration cutting of low alloy steel. *Journal of Materials Processing Technology*, 192-193, 159–165.

- 
- [22] Suzuki, N., Nakamura, A., Shamoto, E., Harada, K., Matsuo, M., & Osada, M. (2003). Ultraprecision micromachining of hardened steel by applying ultrasonic elliptical vibration cutting. *MHS 2003 - Proceedings of 2003 International Symposium on Micromechatronics and Human Science*, 221–226
- [23] Xiao, M., Sato, K., Karube, S., & Soutome, T. (2003). The effect of tool nose radius in ultrasonic vibration cutting of hard metal. *International Journal of Machine Tools and Manufacture*, 43(13), 1375–1382.
- [24] Arjun, P. (2015). Investigation on the chatter vibration and surface texture in vibration assisted micro-milling process. (Master's degree).
- [25] He, P., Li, L., Wang, F., Dambon, O., Klocke, F., Flores, K. M., & Allen, Y. Y. (2014). Bulk metallic glass mold for high volume fabrication of micro optics. *Microsystem Technologies*, 1-7.
- [26] Bakkal, M., Shih, A. J., Scattergood, R. O., & Liu, C. T. (2004). Machining of a Zr–Ti–Al–Cu–Ni metallic glass. *Scripta Materialia*, 50(5), 583-588.
- [27] Bakkal, M. (2009). Electron microscopy of bulk metallic glass machining chips. *Journal of Non-Crystalline Solids*, 355(45), 2220-2223.
- [28] Jiang, M. Q., & Dai, L. H. (2009). Formation mechanism of lamellar chips during machining of bulk metallic glass. *Acta Materialia*, 57(9), 2730-2738.
- [29] Bakkal, M., Shih, A. J., McSpadden, S. B., Liu, C. T., & Scattergood, R. O. (2005). Light emission, chip morphology, and burr formation in drilling the bulk metallic glass. *International Journal of Machine Tools and Manufacture*, 45(7), 741-752.
- [30] Bakkal, M., Shih, A. J., McSpadden, S. B., & Scattergood, R. O. (2005). Thrust force, torque, and tool wear in drilling the bulk metallic glass. *International Journal of Machine Tools and Manufacture*, 45(7), 863-872.
- [31] Bakkal, M., Serbest, E., Karipçin, I., Kuzu, A. T., Karagüzel, U., & Derin, B. (2015). An experimental study on grinding of Zr-based bulk metallic glass. *Advances in Manufacturing*, 3(4), 282-291.
- [32] Bakkal, M., & Nakşiler, V. (2009). Cutting mechanics of bulk metallic glass materials on meso-end milling. *Materials and Manufacturing Processes*, 24(12), 1249-1255.
- [33] Bakkal, M., Nakşiler, V., & Derin, B. (2009). Machinability of bulk metallic glass materials on milling and drilling. In *Advanced Materials Research (Vol. 83, pp. 335-341)*. Trans Tech Publications.
- [34] Foy, K. (2008). Ductile-Regime Machining of Glass Using the Micromilling Process. Retrieved from [http://tigerprints.clemson.edu/all\\_theses](http://tigerprints.clemson.edu/all_theses)
- [35] King, R. F., & Tabor, D. (1954). The Strength Properties and Frictional Behaviour of Brittle Solids. *Proceedings of the Royal Society A: Mathematical, Physical and Engineering Sciences*, 223(1153), 225–238.
- [36] Blackley, W. S., & Scattergood, R. O. (1991). Ductile-regime machining model for diamond turning of brittle materials. *Precision Engineering*, 13(2), 95–103.
- [37] Bifano, T. G., Dow, T. A., & Scattergood, R. O. (1988). Ductile- regime grinding of brittle materials: experimental results and the development of a model. *Advances in Fabrication and Metrology for Optics and Large Optics*, SPIE 966, 108–115.
- [38] Arif, M., Rahman, M., & San, W. Y. (2012). An experimental study on the machining characteristics in ductile-mode milling of BK-7 glass. *International Journal of Advanced Manufacturing Technology*, 60(5-8), 487–495.
- [39] Arif, M., Rahman, M., San, W. Y., & Doshi, N. (2011). An experimental approach to study the capability of end-milling for microcutting of glass. *International Journal of Advanced Manufacturing Technology*, 53(9-12), 1063–1073.
- [40] Neppiras, E. A. (1964). Ultrasonic machining and forming. *Ultrasonics*, 2(4), 167–173.
- [41] Balamuth, L. (1966). Ultrasonic assistance to conventional metal removal. 125(4), 125–130.
- [42] Demishev, G. K., & Kolbasnikova, A. I. (1958). Ultrasonic grinding of glass. *Glass and Ceramics*, 15(3), 131-135.

- 
- [43] Machining, V. A. (2010). *Vibration Assisted Machining: Control and Applications* A thesis submitted for the degree of Doctor of Philosophy by Rasidi Ibrahim. Methodology, (September).
- [44] Brehl, D. E., & Dow, T. A. (2008). Review of vibration-assisted machining. *Precision Engineering*, 32(3), 153–172.
- [45] Thoe, T. B., Aspinwall, D. K., & Wise, M. L. H. (1998). Review on Ultrasonic Machining. *Int. J. Mach. Tools Manufact*, 38(4), 239–255.
- [46] Xu, W. X., & Zhang, L. C. (2015). Ultrasonic vibration-assisted machining: principle, design and application. *Advances in Manufacturing*, 3(3), 173–192.
- [47] Shamoto, E., Suzuki, N., Moriwaki, T., & Naoi, Y. (2002). Development of Ultrasonic Elliptical Vibration Controller for Elliptical Vibration Cutting. *CIRP Annals - Manufacturing Technology*, 51(1), 327–330.
- [48] Zhou, M., Wang, X., Ngoi, B. K. ., & Gan, J. G. (2002). Brittle–ductile transition in the diamond cutting of glasses with the aid of ultrasonic vibration. *Journal of Materials Processing Technology*, 121(2-3), 243–251.
- [49] Ishikawa, K. ichi, Suwabe, H., Nishide, T., & Uneda, M. (1998). Study on combined vibration drilling by ultrasonic and low-frequency vibrations for hard and brittle materials. *Precision Engineering*, 22(4), 196–205.
- [50] Egashira, K., Mizutani, K., & Nagao, T. (2002). Ultrasonic Vibration Drilling of Microholes in Glass. *CIRP Annals - Manufacturing Technology*, 51(1), 339–342.
- [51] Suzuki, N., Haritani, M., Yang, J., Hino, R., & Shamoto, E. (2007). Elliptical vibration cutting of tungsten alloy molds for optical glass parts. *CIRP Annals - Manufacturing Technology*, 56(1), 127–130.
- [52] Gong, H., Fang, F. Z., & Hu, X. T. (2010). Kinematic view of tool life in rotary ultrasonic side milling of hard and brittle materials. *International Journal of Machine Tools and Manufacture*, 50(3), 303–307.
- [53] Klocke, F., & Rübenach, O. (2000). Ultrasonic-assisted diamond turning of glass and steel. *Industrial Diamond Review*, 60(586), 227–239.
- [54] Suzuki, N., Masuda, S., Haritani, M., & Shamato, E. (2004). Ultraprecision micromachining of brittle materials by applying ultrasonic elliptical vibration cutting. *Symposium on Micro-NanoMechatronics and Human Science*, 133–138.
- [55] Yanyan, Y., Bo, Z., & Junli, L. (2009). Ultraprecision surface finishing of nano-ZrO<sub>2</sub> ceramics using two-dimensional ultrasonic assisted grinding. *International Journal of Advanced Manufacturing Technology*, 43(5-6), 462–467.
- [56] Liquidmetal Technologies. Liquidmetal Material Properties. Retrieved from <http://liquidmetal.com/wp-content/uploads/2015/12/LM105-Properties.pdf>
- [57] Physik Instrumente. Specification of LS-180. Retrieved from <http://www.physikinstrumente.com/product-detail-page/ls-180-1202600.html>
- [58] Fischer. Specification of SC 1060-OA. Retrieved from <http://shop.fischerspindle.com/PRECISE/Spindle/SC1060OA>
- [59] Altintas, Y. (2012). *Manufacturing automation: metal cutting mechanics, machine tool vibrations, and CNC design*. Cambridge university press.
- [60] Seah, K. H. W., Li, X., & Lee, K. S. (1995). The effect of applying coolant on tool wear in metal machining. *Journal of materials processing technology*, 48(1), 495-501.
- [61] Ezugwu, E. O., & Bonney, J. (2004). Effect of high-pressure coolant supply when machining nickel-base, Inconel 718, alloy with coated carbide tools. *Journal of Materials Processing Technology*, 153, 1045-1050.
- [62] Dumitrescu, M., Elbestawi, M. A., & El-Wardany, T. I. (2002). Mist coolant applications in high speed machining of advanced materials. *Metal Cutting and High Speed Machining*, 329-339.
- [63] Kishawy, H. A., Dumitrescu, M., Ng, E. G., & Elbestawi, M. A. (2005). Effect of coolant strategy on tool performance, chip morphology and surface quality during high-speed machining of A356 aluminum alloy. *International Journal of Machine Tools and Manufacture*, 45(2), 219-227.

- 
- [64] Physik Instrumente. Specification of P844.10. Retrieved from <http://www.physikinstrumente.com/product-detail-page/p-844-101210.html>
- [65] Lion precision. Specification of CPL-290. Retrieved from [http://www.lionprecision.com/manuals/manual-pdfs/CapEliteSeriesManual\\_LionPrecision.pdf](http://www.lionprecision.com/manuals/manual-pdfs/CapEliteSeriesManual_LionPrecision.pdf)
- [66] ESCO optics. Specification of BK-7 optical glass. Retrieved from <http://escooptics.com>
- [67] Yoshino, M., Aoki, T., Sugishima, T., & Shirakashi, T. (1999). Scratching test on hard-brittle materials under high hydrostatic pressure. *Seimitsu Kogaku Kaishi/Journal of the Japan Society for Precision Engineering*, 65(10), 1481–1485.

---

VITA

Boyuan Xie

Candidate for the Degree of

Master of Science

Thesis: INVESTIGATION ON THE MACHINABILITY IN THE MICRO-MILLING  
OF AMORPHOUS MATERIALS

Major Field: Mechanical & Aerospace Engineering

Biographical:

Education:

Completed the requirements for the Master of Science in Mechanical & Aerospace Engineering at Oklahoma State University, Stillwater, Oklahoma in July, 2015.

Completed the requirements for the Bachelor of Science in Mechanical Engineering & Automation + Software at Dalian JiaoTong University, Dalian, Liaoning, China in July 2010.

Experience:

Research and Teaching Assistant at Oklahoma State University, Stillwater, Oklahoma from January 2014 to July 2016

Manufacturing Engineer at Nanjing Railway New Technology Company Limited, Nanjing, Jiangsu, China from August 2010 to May 2012